
Pro gradu -tutkielma

Fysiikan suuntautumisvaihtoehto

# STIFFER OPTICAL TWEEZERS THROUGH REAL-TIME FEEDBACK CONTROL

Heikki Ojala

11.12.2007

Ohjaajat: M.Sc. Anders Wallin, Doc. Edward Hæggström

Tarkastajat: Doc. Edward Hæggström, Prof. Heimo Saarikko

HELSINGIN YLIOPISTO
FYSIKAALISTEN TIETEIDEN LAITOS

PL 64 (Gustaf Hällströmin katu 2)
00014 Helsingin yliopisto

HELSINGIN YLIOPISTO – HELSINGFORS UNIVERSITET – UNIVERSITY OF HELSINKI

| Tiedekunta/Osasto – Fakultet/Sektion – Faculty/Section | Laitos – Institution – Department | |
|---|---|---|
| Matemaattis-luonnontieteellinen tiedekunta | Fysikaalisten tieteiden laitos | |
| Tekijä – Författare – Author | | |
| Ojala, Heikki Viljami | | |
| Työn nimi – Arbetets titel – Title | | |
| Stiffer Optical Tweezers through Real-Time Feedback Control | | |
| Oppiaine – Läroämne – Subject | | |
| Fysiikka | | |
| Työn laji – Arbetets art – Level | Aika – Datum – Month and year | Sivumäärä – Sidoantal – Number of pages |
| Pro gradu –tutkielma | joulukuu 2007 | 36 + 15 |


Tiivistelmä – Referat – Abstract

Tässä tutkielmassa optisiin pinsetteihin yhdistetään takaisinkytkentä. Tavoitteena on pienentää varianssia, joka on optisilla pinseteillä kiinnipidetyn pallon paikassa. Pienempi varianssi tarkoittaa suurempaa pinsettien jäykkyyttä. Optisia pinsettejä ohjataan akusto-optisilla deflektoreilla ja ohjaus algoritmi on ohjelmoitu field-programmable gate array –kortille. Kun paikan stabiloiva takaisinkytkentä on päällä, pinsettien efektiivinen jäykkyys kasvaa 12.1 -kertaiseksi verrattuna jäykkyyteen ilman takaisinkytkentää. Suurempi jäykkyys mahdollistaa paremman kontrollin kiinnipidetystä pallosta kuin ilman takaisinkytkentää eikä optisten pinsettien laserin tehoa tarvitse nostaa.



Avainsanat – Nyckelord – Keywords

optiset pinsetit, takaisinkytkentä, FPGA, AOD

Säilytyspaikka – Förvaringställe – Where deposited

Kumpulan tiedekirjasto

Muita tietoja – Övriga uppgifter – Additional information

HELSINGIN YLIOPISTO – HELSINGFORS UNIVERSITET – UNIVERSITY OF HELSINKI

| Tiedekunta/Osasto – Fakultet/Sektion – Faculty/Section | Laitos – Institution – Department |
|---|---|
| Faculty of Science | Department of Physical Sciences |

Tekijä – Författare – Author
Ojala, Heikki Viljami

Työn nimi – Arbetets titel – Title
Stiffer Optical Tweezers through Real-Time Feedback Control

Oppiaine – Läroämne – Subject
Physics

| Työn laji – Arbetets art – Level | Aika – Datum – Month and year | Sivumäärä – Sidoantal – Number of pages |
|---|---|---|
| Master's Thesis | December 2007 | 36 + 15 |

Tiivistelmä – Referat – Abstract
This thesis integrates real-time feedback control into an optical tweezers instrument. The goal is to reduce the variance in the trapped bead's position, -effectively increasing the trap stiffness of the optical tweezers. Trap steering is done with acousto-optic deflectors and control algorithms are implemented with a field-programmable gate array –card. When position clamp feedback control is on, the effective trap stiffness increases 12.1-times compared to the stiffness without control. This allows improved spatial control over trapped particles without increasing the trapping laser power.

Avainsanat – Nyckelord – Keywords
optical tweezers, position clamp, feedback, FPGA, AOD

Säilytyspaikka – Förvaringställe – Where deposited
Kumpula Science Library

Muita tietoja – Övriga uppgifter – Additional information

# Table of Contents

# 1 Introduction

Optical forces can trap and manipulate micron-sized objects. Optical tweezers utilize the high-intensity electric field from a laser source to achieve stable trapping of dielectric spheres in three dimensions[1]. High intensity and a steep intensity gradient, which enable trapping, are achieved using a microscope with a high numerical aperture objective. Pico-Newton Forces and sub-nanometer displacement can be measured using optical tweezers[2].

Optical tweezers have found a wide range of applications in biophysical experiments. Traditional imaging methods like X-ray crystallography and nuclear magnetic resonance imaging can be used to study the structure of biomolecules. However these techniques can't reveal the dynamics of the molecules under study. Optical tweezers bring valuable insight into the dynamics and the mechanics of biomolecules. For example, optical tweezers have been used to study mechanical properties of DNA molecules, RNA polymerases and other molecular motors and protein folding transitions[3, 4]. The advantages of optical tweezers over other single molecule techniques are the force range, that is well suited for biological systems, and the high-resolution in the force and position measurements[5].

Control is used to make a device respond in a desired way. It can also be used to improve the performance of a system. In the atomic force microscope (AFM) feedback allows imaging samples without damaging them. Different feedback algorithms can be used to improve the AFM scanning speed[6].

Environmental disturbances in a measurement system can be minimized using feedback control. Already in the very first optical tweezers instrument Ashkin used feedback control when levitating particles[7]. He used an electro-optical modulator to control the optical power. The error signal from two photodetectors was amplified with analog circuitry to drive the modulators. The achieved bandwidth was 10 kHz. Simmons *et. al* used acousto-optic modulators (AOM) to steer the trap[8]. They used amplifiers and voltage controlled oscillators to close the feedback loop from a quadrant photodetector to the AOM. The bandwidth of the electronics was 5 kHz and the beads (1 μm in diameter) were trapped using 52 mW laser power (40 pN/μm stiffness). They claimed that the feedback improved the trap stiffness by a factor of 400, but these results have not been reproduced. Ranaweera used computer simulations to predict the effect of position clamp proportional control[9]. He found, that with proportional feedback control, the bead position variance was 49 times smaller than in the open loop case. He used 0.01 ms sampling time, 10 pN/μm trap stiffness and 1 μm bead diameter as simulation parameters. Wulff *et. al* used fast steering mirrors to control their instrument[10]. The bandwidth of their control system was 150 Hz and they could reduce the root mean square displacement by 20% when frequencies above 100 Hz were filtered out. The laser power was 100 mW whereas the bead diameter was 1 μm. Pilizota *et. al* used a digital signal processing board to make an angle clamp to measure rotary molecular motors[11]. They controlled bead pair angles with 2° resolution with 18 mW laser power and 0.5 μm diameter beads. The instrument bandwidth was 1.6 kHz.

One disadvantage of optical tweezers is laser optical damage to active biological systems[5], and laser induced solution heating[12]. Therefore the trapping laser wavelength is usually selected to be in the infra-red range so that proteins are transparent to the trapping light, and so that the light is not absorbed by the solution. Reduced laser power minimizes the optical damage but decreases the trap strength

which increases position fluctuations. To avoid this drop in trap strength one can use feedback control.

The aim of this work is to integrate a feedback loop into the optical tweezers instrument at the Electronics Research Unit/University of Helsinki[13, 14]. Trap steering is done with AODs. Detection is done using a position sensitive detector and back-focal-plane interferometry[15]. Data-acquisition is handled with a field-programmable gate array (FPGA) –card. The FPGA card performs the calculations of the feedback algorithm and controls direct digital synthesizers (DDS). These DDSs drive the AODs. Position clamp feedback control is then used to increase the effective trap stiffness of the optical tweezers.

This thesis first considers optical trapping theory. This is followed by the theory of back-focal plane detection and the theory of steering with AODs. A calibration procedure for the AODs and the position detector is presented. The power spectral density of a bead in a feedback controlled trap is derived.

Design and construction of the feedback controlled optical tweezers is shown in section 3. In section 4 the results from the calibration and the position clamp feedback control are shown. This is followed by a discussions in section 5 and conclusion in section 6.

The work of this thesis has been presented at three conferences:

1. Ojala, H. Korsbäck, A., Wallin, A. and Hæggström, E., (2007), "*Stiffer Optical Tweezers With Feedback Control*", 41th Physics Days of the Finnish Physical Society, Tallinn, Estonia.
2. Wallin A.E. and Ojala H. (2007) "*FPGA-Based Real-Time Feedback Control of Optical Tweezers*", National Instruments NIWeek Paper Contest entry. Selected as the contest winner in the Biotechnology and Life Sciences category[16]
3. Wallin, A.E., Ojala, H., Korsbäck, A., Tuma, R., and Hæggström E., *Real-time control of optical tweezers.* Proceedings of SPIE, 2007. **6644**: p. 66441Y.

# 2 Theory

In this section the physics of optical trapping is shortly explained in the Rayleigh regime, where the radius of the bead $a \ll \lambda$ the wavelength of the light. Position detection using back-focal-plane interferometry[15, 17] and position sensitive detectors (PSD) is presented, and the functioning of acousto-optic deflectors (AOD) is explained. At the end, calibration methods for the optical tweezers instrument are given and the effect of feedback control is explained using the power spectrum method.

## 2.1 Optical trapping

The force induced by the electromagnetic field of laser light on a bead (radius $a$) arises from two parts, 1) the scattering force and 2) the gradient force. The scattering force is the change in bead momentum when radiation is absorbed from one direction and scattered in all directions. This pushes the bead in the direction of light propagation. The force is directly proportional to the laser intensity $I$ [2]

$$F_{scatt} = \frac{I\sigma n_m}{c}, \tag{1}$$

$$\sigma = \frac{128\pi^2 a^6}{3\lambda^4}\left(\frac{m^2-1}{m^2+2}\right)^2,$$

where $n_m$ is the index of refraction in the medium, $c$ is the speed of light, $m$ is the ratio between the index of refraction of the bead and the medium and $\lambda$ is the wavelength of the laser.

The gradient force is due to the high intensity gradient in the field. This gradient is generated by focusing the laser beam steeply with a high numerical aperture (NA) objective. Treating the bead as a dipole, induced by the light field, the Lorentz force acting on the bead gives the gradient force[1]

$$F_{grad} = \frac{\alpha_p}{2}\nabla < E^2 >, \tag{2}$$

$$\alpha_p = {n_m}^2 a^3\left(\frac{m^2-1}{m^2+2}\right),$$

where $\alpha_p$ is the polarizability of the bead and the time average of the square of the electric field is proportional to the intensity ($I = \varepsilon_0 c < E^2 >$ [18]).

The gradient force alone would trap the bead in the focal point of the objective. But, because of the scattering force, trapping happens slightly beyond the focus depending on the strength of the gradient defined by the NA of the objective.

## 2.2 Position Detection

The electric field on a detector (Figure 1) can be derived by assuming Gaussian intensity profile for the laser beam. A trapped bead in the focal plane ($\vec{r}_s = x\hat{i} + y\hat{j}$) can be treated as a Rayleigh scatterer induced by the laser. The unscattered field from the

laser $E(\vec{r})$ and the scattered field from the bead $E'(\vec{r})$ produce an interference field on the detector. The change in intensity is

$$\delta I = \frac{\varepsilon_s c_s}{2}\left(\left|E+E'\right|^2 - \left|E\right|^2\right) \approx \varepsilon_s c_s \,\mathrm{Re}(EE'^*)\,, \tag{3}$$

where $\left|E'\right|^2$ can be neglected, because the field at the detector from the bead is small compared to the unscattered field[15]. Integrating over the relevant detector area gives the signal from the detector. For example in the x-direction

$$\frac{\delta I_x}{I} = r^2 \int_{-\pi/2}^{\pi/2} d\phi \int_0^{\theta_{\max}} d\theta \sin\theta \, \delta I \,. \tag{4}$$

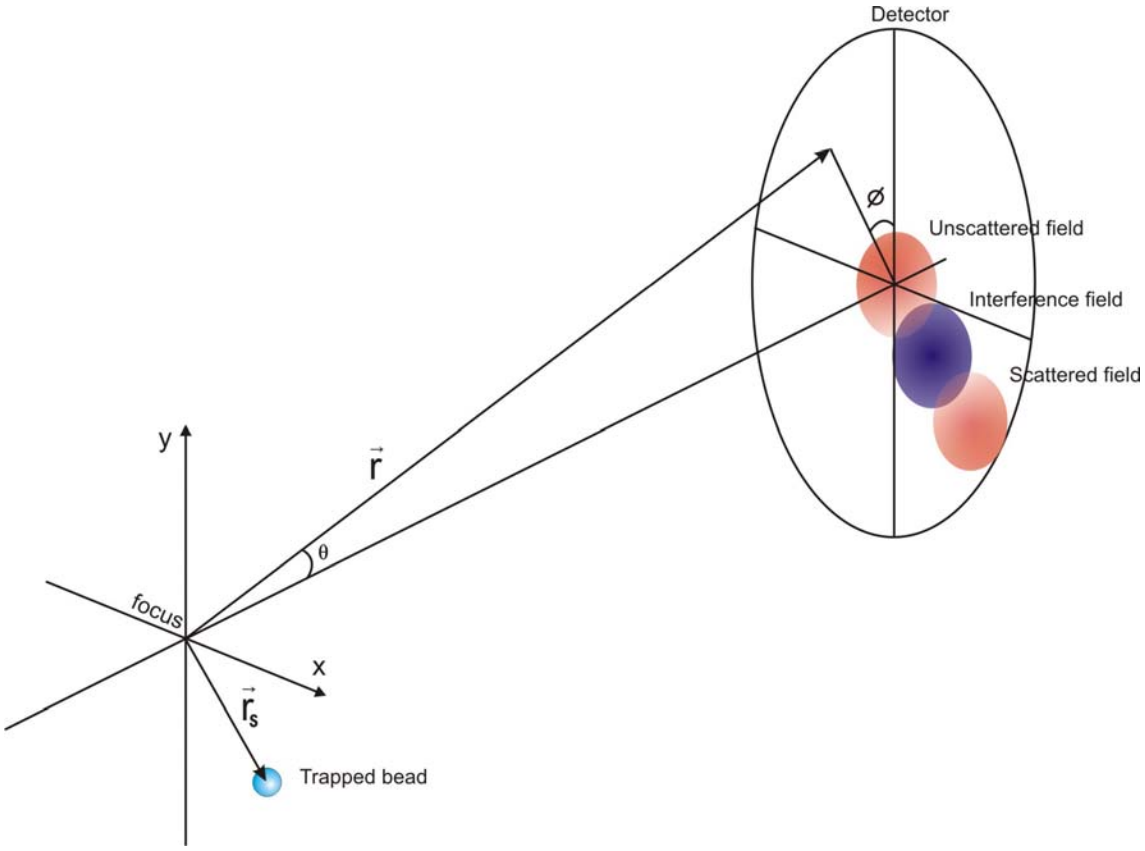


**Figure 1. Laser polarizes the trapped bead and the interference between scattered field and the field that passes straight through (unscattered field) gives the detection signal (interference field).**

The overall intensity on the one half of the detector is $I_{x+} \equiv I/2 + \delta I_x$. The voltage signal from a position sensitive detector (PSD) is proportional to the relative intensities in the detector area[19]

$$V_x \propto \frac{I_{x+} - I_{x-}}{I_{x+} + I_{x-}} \equiv \frac{I/2 + \delta I_x - \left(I/2 - \delta I_x\right)}{I/2 + \delta I_x + \left(I/2 - \delta I_x\right)} = 2\frac{\delta I_x}{I}. \tag{5}$$

So, the voltage signals depend on the trapped bead's displacement (x, y) as[15]

$$\begin{pmatrix} V_x \\ V_y \end{pmatrix} \propto \begin{pmatrix} x \\ y \end{pmatrix} \exp\left(-\frac{x^2+y^2}{w^2}\right), \tag{6}$$

where $w$ is the focal beam width. The theoretical voltage signals for different bead positions are plotted in Figure 2 using a beam width of 0.415 µm.

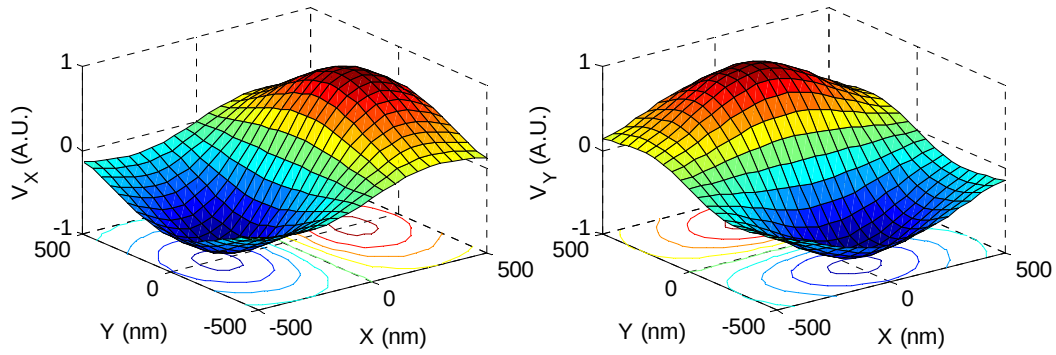


**Figure 2. Voltage signals from the PSD from eq. 6.**

## 2.3 Steering

An acousto-optic deflector (AOD) is used to steer the laser beam. Acoustic waves propagating through a crystal create a periodic change in the index of refraction. These act like a moving phase grating and diffract light that is passing through the crystal. In isotropic media when the momentum mismatch between the acoustic wave and the light wave is zero, light is only diffracted to the first maximum. This is true when the incoming beam is in the Bragg-angle $\theta_B$

$$\sin\theta_B = \frac{\lambda f_{AOD}}{2V}, \qquad (7)$$

where $\lambda$ is the wavelength of the light in the crystal, $f_{AOD}$ is the acoustic frequency and $V$ is the acoustic phase velocity. The diffracted beam is deflected an angle $2\theta_B$ from the incident beam[20] as shown in Figure 3.

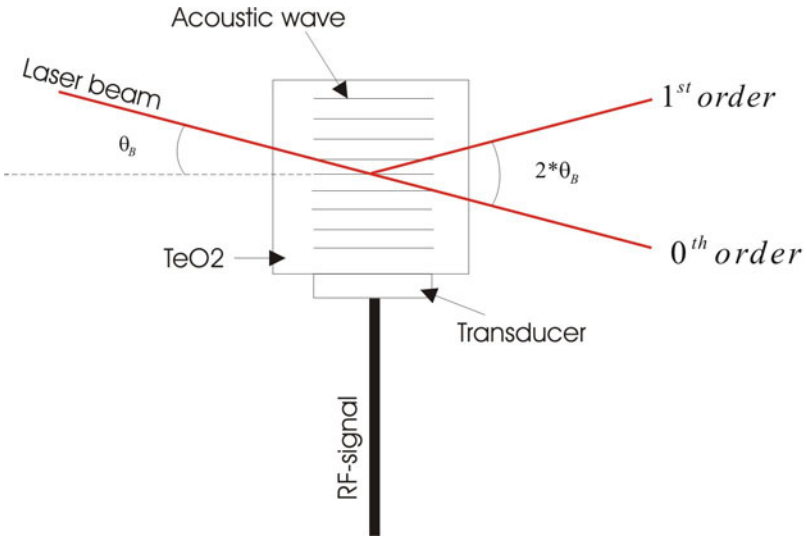


**Figure 3. Laser beam (red) deflected inside the crystal. If the incoming angle ($\theta_B$) relative to the acoustic wave equals the Bragg angle, only a 1st order maximum results.**

The intensity of the diffracted light depends on the acoustic wave power and the material parameters of the AOD crystal[21]. Equation 7 defines the Bragg angle where only one diffracted beam is created. When steering the trap the acoustic frequency is changed. This alters the Bragg angle and affects the diffracted light intensity. The acoustic bandwidth, defined as the frequency range where the drop in the diffracted light intensity is less than 3 dB, can be widened using a birefringent material[21].

In the small angle approximation the AOD deflection angle is linearly proportional to the driving frequency (Eq.7). Trap position $x_{trap}$ is then proportional to the driving frequency

$$x_{trap} = \alpha \, f_{AOD} \,. \tag{8}$$

The acoustic bandwidth of the AOD used in this work is 20 MHz. This corresponds to 32 mrad beam deflection. In the optical path after the AODs there is a 3× beam expander and an objective with a focal length of 2 mm. These components generate a theoretical value of $\alpha$

$$\alpha = \frac{32 \cdot 10^{-3}}{20\ MHz} \frac{2\ mm}{3} = 1.066\ \mu m / MHz \,.$$

The correspondence between the deflection and the trap focus movement is shown in Figure 4 using the ray-transfer matrix method[18] for geometrical optics ray-tracing.

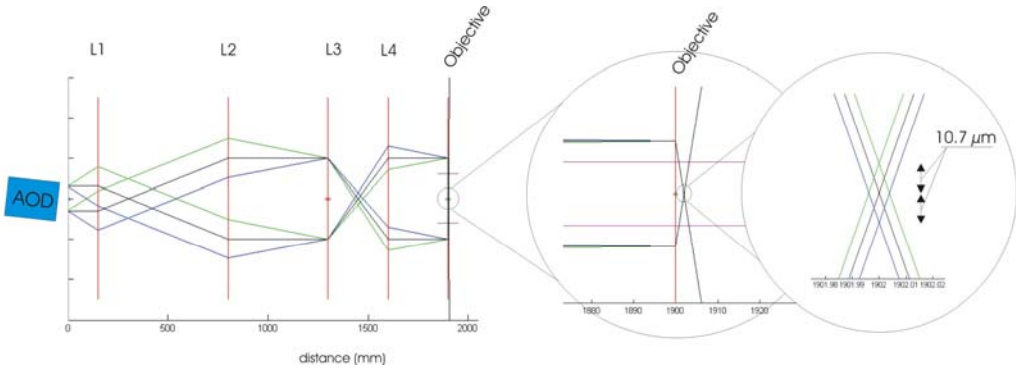


**Figure 4. Beam deflection in the AOD translates the focus in the sample plane. Three beams are shown; one going straight ( $f_{AOD} = 35$ MHz, black), one with 0.016 mrad deflection angle ( $f_{AOD} = 45$ MHz, green) and one with -0.016 mrad deflection angle ( $f_{AOD} = 25$ MHz, blue). After the telescopes (L1, L2 and L3, L4) and the objective these beam movements laterally displace (± 10.7 µm) the focus in the sample plane.**

## 2.4 Calibration

Methods to calibrate the optical tweezers are introduced next. First the proportionality between the AOD frequency and the position is explained. Then the relationship between PSD voltages and bead position is elucidated.

### 2.4.1 Particle tracking

The proportionality constant between the AOD driving frequency and the trap position is determined by first calibrating the video image and then measuring the positions of a trapped bead from the video screen.

To get the bead position the image of the bead is first filtered with a boxcar average to get rid of the background. Then the noise in the image is suppressed by convolving the

image with a Gaussian surface. Both operations are handled with a single convolution kernel[22]

$$K(i,j)=\frac{1}{K_0}\left[\frac{1}{B}e^{-\frac{i^2+j^2}{4\lambda_n^2}}-\frac{1}{(2w_b+1)^2}\right], \tag{9}$$

$$K_0=\frac{1}{B}\left[\sum_{i=-w_b}^{w_b}e^{-\frac{i^2}{2\lambda_n^2}}\right]^2-\frac{B}{(2w_b+1)^2},$$

$$B=\left[\sum_{i=-w_b}^{w_b}e^{-\frac{i^2}{4\lambda_n^2}}\right]^2,$$

where $i$ and $j$ are the pixel indices, $w_b$ is an integer larger than the apparent bead radius in pixels and $\lambda_n$ is the half width of the Gaussian surface, -usually set to unity. From the filtered image the locally brightest pixel at $(x,y)$ is found. This position is then used to find the geometric center $(x_0,y_0)$

$$(x_0,y_0)=(x+\varepsilon_x,y+\varepsilon_y), \tag{10}$$

$$\begin{pmatrix}\varepsilon_x\\ \varepsilon_y\end{pmatrix}=\frac{1}{m_0}\sum_{i^2+j^2\le {w_b}^2}\begin{pmatrix}i\\ j\end{pmatrix}A(x+i,y+j),$$

$$m_0=\sum_{i^2+j^2\le {w_b}^2}A(x+i,y+j),$$

where $A$ is the image and the summations are done for pixels closer than $w_b$ pixels away from the brightest pixel $(x,y)$. Now, using the bead center $(x_0,y_0)$ as the trap position, the proportionality between the trap position and the AOD frequency can be resolved.

### 2.4.2 Surface fit for the PSD signal

Theoretically the functional dependence of the detector signal on bead position is derived in Eq.6. However, for position detector calibration, a function must be fitted to the PSD voltages to get the bead displacement relative to the detection beam

$$x_{bead}=\sum_{i,j=0}^{n}b_{ij}V_X^iV_Y^j. \tag{11}$$

Depending on the required accuracy the value of $n$ can be chosen. Equation 11 is fitted to a small region around the detection laser focus where the inverse of Eq.6 is single-valued.

## 2.5 Trapped bead in a position clamp

For micron sized objects the Reynold's number is typically small[1]. Additionally the bead inertia can be neglected. Then the Langevin equation describes the trapped bead motion in a harmonic potential

$$\beta\,\dot{x}(t) + k\big(x(t) - x_{trap}(t)\big) = F_T(t)\,, \qquad (12)$$

where $\beta = 6\pi\eta a$ is the Stokes friction factor with $\eta$ as the dynamic fluid viscosity and $a$ the bead radius. $F_T(t)$ is the Brownian thermal force, $k$ is the spring constant of the trap and $x$ and $x_{trap}$ are the position of the bead and the trap, respectively. If the trap position is constant and set to zero the classical Lorentz-spectrum is obtained for spatial frequencies of the bead displacement[1, 2, 23]

$$\left|\tilde{x}(f)\right|^2 = \frac{D}{\pi^2\left(f_C^2 + f^2\right)}\,, \qquad (13)$$

where $f_C = k(2\pi\beta)^{-1}$ is the corner frequency and $D = \dfrac{k_B T}{\beta}$ is the diffusion constant from Einstein's equation. A time-series of the thermal motion of the bead can be measured, and the power-spectrum calculated. Fitting Eq.13 to the power-spectrum and determining $f_C$ determines the trap stiffness.

Instead of setting $x_{trap}$ to zero, feedback control can be used. The simplest controlling algorithm i.e. proportional feedback control is selected. The bead position at some previous time $t-\tau$ then defines the trap position at time $t$ $x_{trap}(t) = K_p\big(x_{set} - x(t-\tau)\big)$, where $K_p$ is the feedback gain and $x_{set}$ is the set-point of the loop (Figure 5).

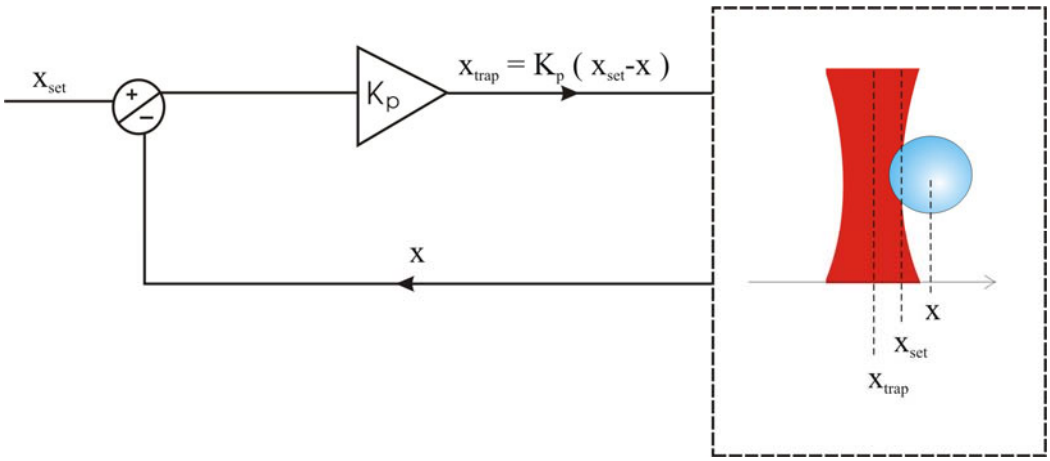


**Figure 5. Position clamp feedback control. The set point ($x_{set}$) is subtracted from the current bead position (x). The result is multiplied by the gain factor ($K_p$) and used to steer the trap ($x_{trap}$).**

Using the trap position in Eq.12 and fixing the set point to zero gives

$$\beta\,\dot{x}(t) + k\big(x(t) + K_p x(t-\tau)\big) = F_T(t)\,. \qquad (14)$$

---

[1]The Reynolds number for a typical bead of radius a=0.5 μm and velocity $v$=1 mm/s with viscosity and density of water as η=0.001 Pa·s and ρ=1000 kg/m$^3$ respectively is $\mathrm{Re} = \dfrac{va\rho}{\eta} = 5\cdot 10^{-4}$.

Fourier transforming Eq.14 gives

$$i2\pi f\beta\,\tilde{x}(f) + k\tilde{x}(f) + kK_p \exp(-i2\pi f\tau)\tilde{x}(f) = \tilde{F}_T(f). \qquad (15)$$

Solving this for $\tilde{x}$ gives the power spectrum of a trapped bead with proportional feedback control

$$\left|\tilde{x}(f)\right|^2 = \frac{\left|\tilde{F}_T(f)\right|^2}{\left|i2\pi f\beta + kK_p \exp(-i2\pi f\tau) + k\right|^2}. \qquad (16)$$

The power spectrum for the thermal force is a constant $\left|\tilde{F}_T(f)\right|^2 = 4k_B T\beta$ (white noise), where $k_B$ is the Boltzmann's constant and $T$ is the temperature. The power spectrum is then

$$S(f) \equiv \left|\tilde{x}(f)\right|^2 = \frac{4D}{\left|i2\pi f + \frac{k}{\beta}K_p \exp(-i2\pi f\tau) + \frac{k}{\beta}\right|^2}. \qquad (17)$$

This is similar to the equation presented by Gosse *et. al*[24] for feedback controlled magnetic tweezers, but their system had zero stiffness without active control.

There are two corrections to this theory. First, the position detector system is usually a low-pass filter that modifies the expected power spectrum[23, 25, 26]

$$C^{(diode)}(f) \equiv \frac{S^{(filtered)}(f)}{S(f)} = (\alpha^{(diode)})^2 + \frac{1-(\alpha^{(diode)})^2}{1+\left(\frac{f}{f_{3dB}^{(diode)}}\right)^2}, \qquad (18)$$

where $(\alpha^{(diode)})$ and $f_{3dB}^{(diode)}$ are parameters defining the detector which can be used in fitting. Second, aliasing in the data-acquisition system can be taken into account by summing over the aliased frequencies[23]

$$S^{(aliased)}(f) = \sum_{n=-\infty}^{\infty} S^{(filtered)}(f + nf_{sample}), \qquad (19)$$

where $f_{sample}$ is the sampling frequency. Combining Eqs.17, 18 and 19 gives

$$S(f) = \sum_{n=-\infty}^{\infty} \frac{4D\,C^{(diode)}(f + nf_{sample})}{\left|i2\pi(f + nf_{sample}) + \frac{k}{\beta}K_p \exp(-i2\pi(f + nf_{sample})\tau) + \frac{k}{\beta}\right|^2}. \qquad (20)$$

This is the expected power spectral density which will be fit to the experimental data.

The proportional control reduces the mean-square fluctuations of the bead. An effective trap stiffness $k_{eff}$ can be defined using the equipartition theorem[24]

$$< x^2 >= \int_0^{\infty} S(f)df = \frac{k_B T}{k_{eff}}. \qquad (21)$$

Eq.20 can be integrated numerically to get the resulting mean-square of the position.

# 3 Materials and methods

## 3.1 Optics

Our steerable optical tweezers are built around an inverted microscope (Nikon Eclipse TE2000-U), Figure 6. Trapping is done with a continuous wave laser (Coherent Compass 4000, wavelength 1064 nm) whose output power can be controlled up to 4 W. At the output of the laser is a collimating telescope (L5, L6). The laser is isolated with a Faraday isolator (ISO1, Linos, FI-1060-5SI) to restrict beam reflections from re-entering the laser. Subsequently the beam is expanded three-fold with a 1:3 telescope (L1, L2) to overfill the objective aperture. The mid-point of the two AODs is imaged onto the back-aperture of the objective with a 1:1 telescope lens system (L3, L4). A 100× objective (Nikon, Plan Fluor) with 1.3 numerical aperture is used.

To detect the movements of a trapped bead using back-focal-plane interferometry (Section 2.2) a detection laser (830 nm FTEC-0830-P20-P-FQ, Blue Sky Research) is employed. A Faraday isolator (ISO2, DLI-1, Linos) prevents optical feedback. The beam from the detection laser is combined with the trapping beam using a dichroic mirror (D1) (SWP-45-RU1064-TU850-PW-2025-C, CVI Laser, Appendix A). On the condenser side the back-focal plane is imaged onto a position sensitive detector (S2-0171, Sitek). Signals from the detectors are amplified with instrumentation amplifiers (INA111, Appendix B). A laser-line bandpass filter (F1, FL830-10, Thorlabs, Appendix A) transmits only 830 nm light and prevents trapping light from reaching the detector. A broadband dielectric mirror (D3, BB2-E03, Thorlabs, Appendix A) transmits visible light but deflects trapping light towards the detector.

Trapping and detection beams are directed to the sample space with a dichroic mirror (D2, 780dcspxr, Chroma, Appendix A) so that the image of the experiment can be viewed with a CCD camera (Panasonic CCTV Camera, WV-BP100/G) connected to the front-port of the microscope. A mercury arc-lamp (Nikon) provides illumination for the camera. Filters that block NIR-wavelengths (F2, KG1 and KG3 glass, Schott Optik, Appendix A) are used in front of the CCD to totally or partially block trapping/detection beams from reaching the camera.

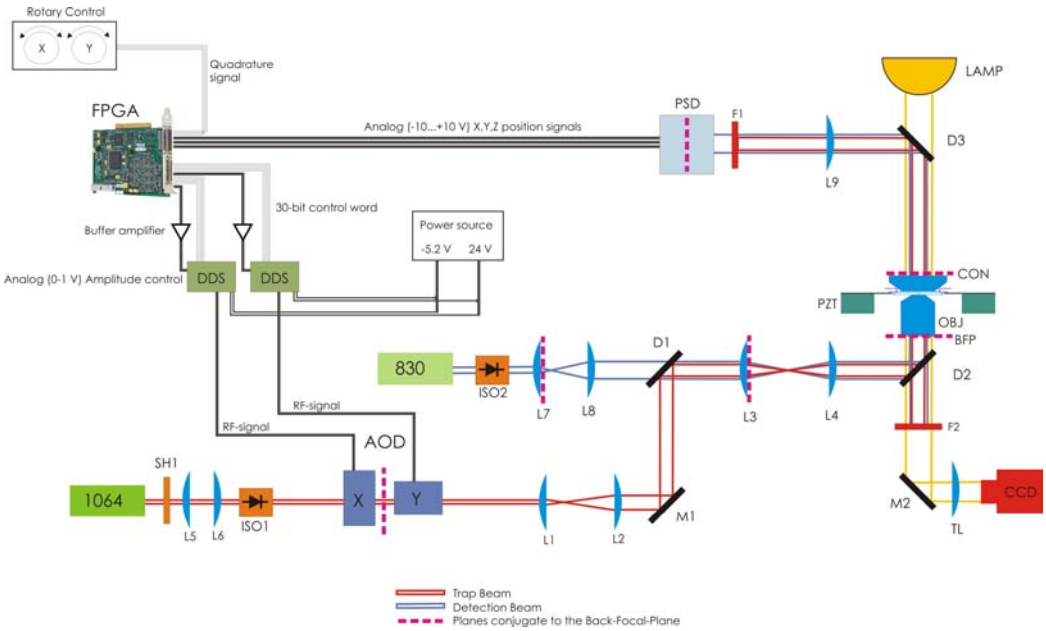


**Figure 6. Overview of the optical tweezers instrument. See text for explanations. Components: trapping laser (1064), detection laser (830), optical isolator (ISO), lens (L), mirror (M), dichroic mirror (D), shutter (SH), piezo stage (PZT), objective (OBJ), condenser (CON), filter (F), position sensitive detector (PSD), field-programmable gate array (FPGA) and direct digital synthesizers (DDS)**

## 3.2 Acousto Optic Deflector (AOD)

Steering is accomplished with two AODs (45035-3-6.5deg-1.06-xy, NEOS-Technologies) mounted at right angles to each other. They allow steering in both x and y direction. The AODs used in this work are made of paratellurite ($TeO_2$). This birefringent material makes the acoustic bandwidth larger than in the isotropic case[21]. A piezo-electric $LiNbO_3$ transducer emits a slow shear wave[2][27] into the crystal (3x3 mm aperture). The speed of sound in the crystal is 660 m/s which implies a maximum update time of $\frac{3\text{ mm}}{0.66\text{ mm}/\mu s} = 4.5\ \mu s$. The acoustic wave is launched 6.5° off the <110> direction. This makes the deflection efficiency flat over the entire acoustic bandwidth[28] (See section 4.1, AOD diffraction efficiency). Mounting of the AODs is shown in Figure 7. The AODs are controlled with direct digital synthesizers (DDS) which generate the required RF-signal.

[2] In a shear wave the displacement of the medium is perpendicular to the direction of propagation. In the <110> direction (in $TeO_2$) shear wave velocity is 5 times slower than in the <100> direction.

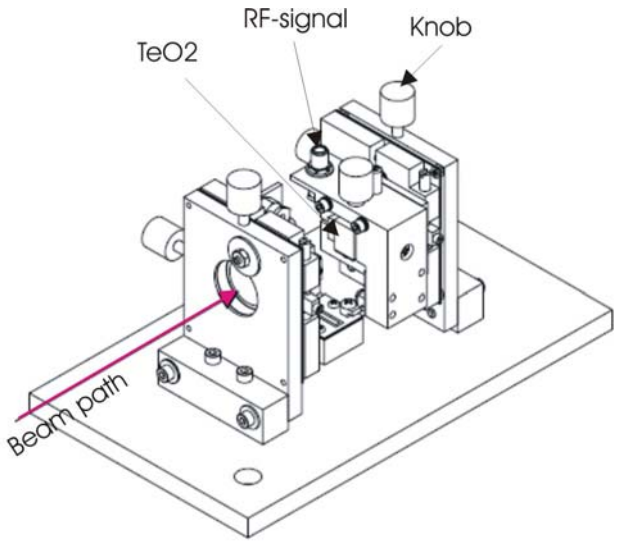


**Figure 7. Mounting of the AOD crystals. Note the knobs which are used to rotate the crystals so that the incoming beam hits the crystal at Bragg angle. (Image from NEOS technologies product manual[29])**

## 3.3 Direct digital synthesizer (DDS)

To control the AODs direct digital frequency synthesizers (64010-20022AMDFS, Neos Technologies) are used. Direct digital synthesis means that inside the DDS there is a look-up table (LUT) where the desired waveform is stored in digitized form. In this case the waveform is a sine wave. The synthesizer cycles through the points stored in the table outputting them to a digital-to-analog converter (DAC) -generating the output radio frequency (RF) signal. The output frequency is controlled with a 30-bit digital input word. The points stored in the LUT can be seen as points on a unit circle. The control word defines the phase change on the unit circle between two adjacent values sampled by the DAC. In other words, the more values gone through by the DAC the slower the output frequency. The DAC samples values at the internal clock frequency (1 GHz for our device).

Our DDS can supply RF output up to 2 W of continuous wave power across a 10 MHz to 200 MHz band with an internal clock frequency of 1 GHz. Because the AOD is used at frequencies between 25 and 45 MHz, the bandwidth of the DDS suffices. The frequency settling time is less than 40 pulses i.e. at 1 GHz, 40 ns. The output frequency is calculated from the input control word as

$$f_{AOD} = f_0 \cdot \frac{K_{10}}{2^{31}}, \tag{22}$$

where $f_{AOD}$ is the output frequency from the DDS input to the AODs, $f_0$ is the internal clock frequency (1 GHz) and $K_{10}$ is the 30-bit control word in decimal notation. Hence the smallest step that the DDS can take is 0.5 Hz. This corresponds to 1 pm movement of the laser focus in the sample plane. The full range of the laser focus movement corresponds to 25-45 MHz, and equals 21 µm in the sample plane (see Figure 4). The amplitude of the RF-signal is determined by an analog voltage input (0-1 V) to the DDS.

## 3.4 Field-programmable gate array (FPGA)

The 30-bit digital input words (pin outs in Appendix C) to the DDSs are created with a FPGA-card (PCI-7833R, National Instruments, 40 MHz clock rate) with 3 million reprogrammable gates. Using an FPGA it is possible to implement many kinds of steering algorithms (e.g. multiple traps and feedback control) without changing the hardware.

The position signals from the PSD are analog voltages and therefore the FPGA-card features eight analog input channels. The AD conversion is done with a successive approximation[3][30] circuit at 16-bit resolution. The maximum sampling rate is 200 kS/s, of a ±10 V input signal.

The FPGA board features eight analog output channels which use single ended output[4]. These 16-bit-resolution channels allow a maximum update rate of 1 MS/s. The amplitude modulation of the RF-signal is done through these channels. This limits the update rate of the DDS's amplitude modulation to 1 MHz along with the buffer amplifiers (section 3.5) bandwidth (Appendix E). The FPGA hardware overview (Figure 8) also shows the 96 reconfigurable digital input/output gates.

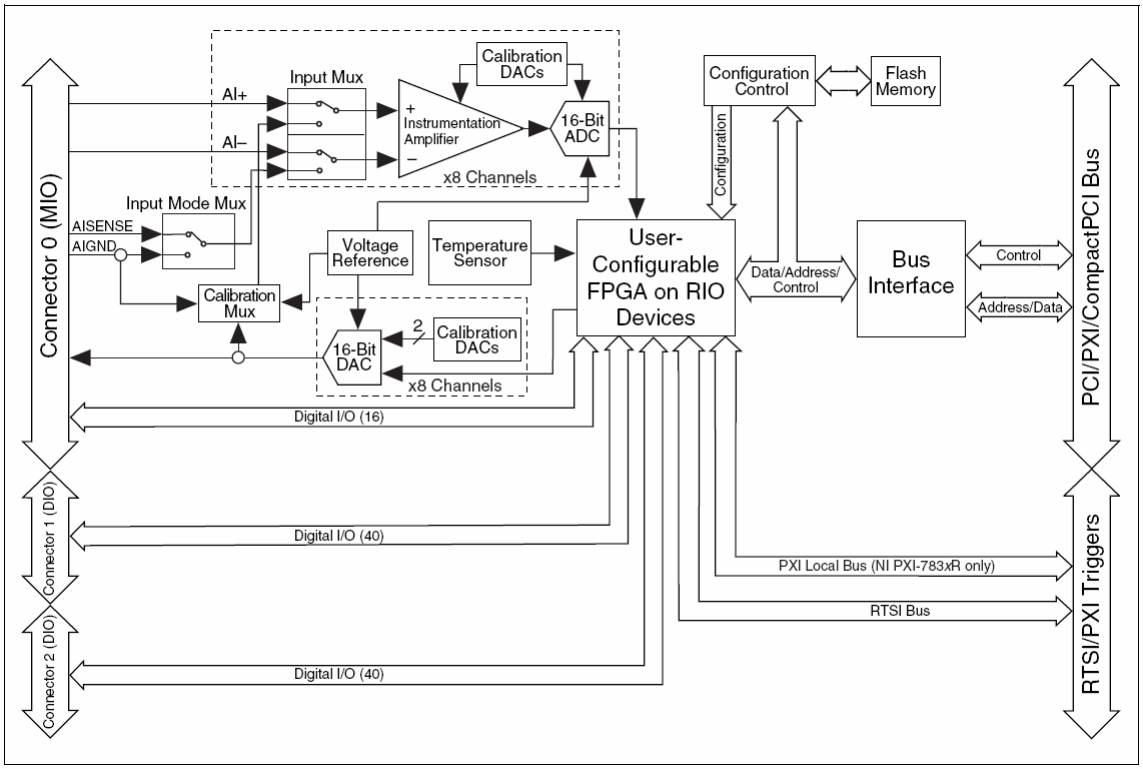


**Figure 8. Overview of the FPGA card (PCI-7833R, National Instruments) hardware. There are 96 reconfigurable digital input/output channels, 8 independent AD converters and 8 independent DA converters (image from National Instruments User Manual[31]).**

[3] In successive approximation conversion (SAC) a comparison between the analog voltage and the digital converted result is done by going through all the bits one by one, starting from the MSB. Each bit is set to zero if the digital value is over the analog voltage, otherwise the bit is set to one. With SAC the conversion time is constant.

[4] Single ended signaling means that all the outputs are connected to common ground reference.

## 3.5 Electronics

A power source was built for the DDSs. Each DDS requires a -5.2 V source capable of two amperes output current and one 24 V source (1 A output current). For 24 V a commercial voltage source was used. To produce the -5.2 volts first the voltage from a wall outlet (50 Hz, 230 VAC) was transformed to 9 VAC. After the transformation the voltage was rectified with a rectifying bridge and filtered with four 4700 µF electrolyte capacitors in parallel. The filtered signal was then regulated to -5.2 V with a negative voltage regulator (LM723), and to ascertain that enough current can be produced the regulator was accompanied by a power transistor (BDX66B). Because of the high currents in the transistor, a heat sink was mounted on top of the transistor. See Appendix B for the schematics and the circuit board for a negative voltage regulator from the LM723.

The DDSs also need an analog modulation voltage between zero and one volt to define the amplitude of the output RF-signal. The input impedance of the analog input on the DDS is 50 Ω, requiring 20 mA current sourcing capability from the driving analog voltage. Because the FPGA card can produce voltages between ±10 V but only 2.5 mA of current, an operational amplifier circuit was used to match the voltage range and increase the current driving capability (schematics and circuit board are shown in Appendix B). This buffer amplifier allows the use of the full precision of the FPGA card's DA converters and it also corrects the impedance mismatch between the FPGA (1.25 Ω output impedance) and the DDS (needs 20 mA of current with 1 V, i.e. impedance of 50 Ω).

The DDSs, power supplies, and buffer amplifiers were housed in the same box together with a 120 mm fan (the synthesizers require cooling). A schematic diagram of this DDS box is shown in Appendix B. Image of the box is shown in Appendix D.

## 3.6 LabVIEW™ programming

The FPGA card is programmed using LabVIEW™ 8.5 and the LabVIEW FPGA module. The LabVIEW code is compiled and downloaded to the FPGA-card. Using LabVIEW no knowledge of VHDL[32] or low-level FPGA programming is needed. Control of the virtual instrument (VI) downloaded to the FPGA can be done either by directly controlling a target VI on the FPGA or by using a different host VI running on the host operating system. The host VI allows the use of floating point algorithms combined with the exact timing of the FPGA. On the FPGA one is limited to use only integer numbers and arithmetics.

### 3.6.1 Program for time sharing

As an example of steering and quick control four time-shared traps were programmed. Time sharing creates multiple traps out of only one laser beam[33]. When the visiting frequency between individual traps is high enough each of the visited positions can be used to trap beads. A LabVIEW program that implements time sharing on the FPGA-card is shown in Figure 9.

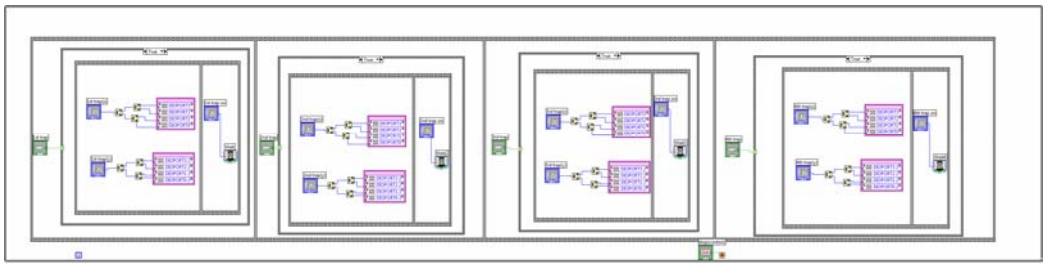

**Figure 9. A Loop of four sequences. Each of them takes in two integers and outputs them to the DDSs as 30-bit digital word. Individual positions are held for a preset time before moving to the next trap.**

### 3.6.2 Program for position clamp feedback control

The control algorithm for the position clamp was a simple proportional feedback control. The program downloaded on the FPGA is shown in Figure 10. The position signal from the PSD is a voltage that is digitized with 16 bit resolution (AI0). This is subtracted from the desired position ($V_{set}$). The resulting 16 bit number is multiplied with an integer (G) corresponding to the needed feedback gain. The result is then used for steering (DIOPORT0-3). Both negative- and positive-gain feedback control is possible using this program.

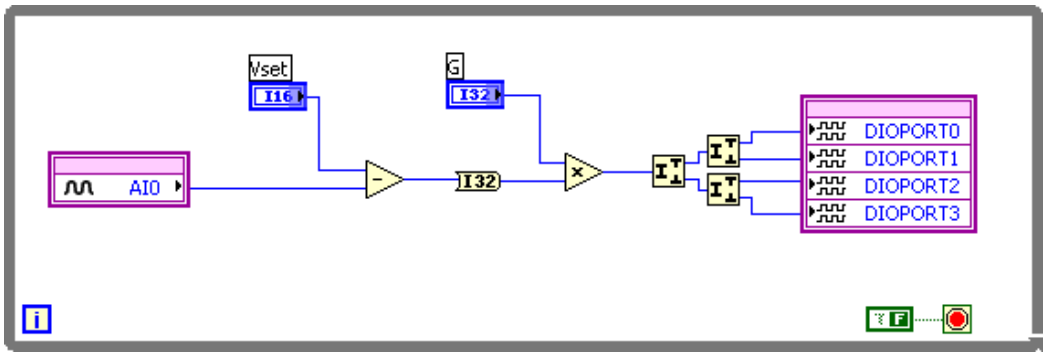


**Figure 10. Feedback loop implemented on the FPGA-card using LabVIEW. The indefinitely running loop reads the measured position signal (AI0, 16 bit), from which the set point (Vset) is subtracted. This is then multiplied with a gain factor (G) and written out into the digital ports (DIOPORT0-3) to be used in DDS to control the AOD and steer the laser beam. The control word to the DDS is 30-bit so the two most significant bits aren't used when the word is written to the DDS. There are two of these loops to control both y- and x- axis.**

### 3.6.3 Program for manual control

Before feedback control can be turned on the trapped bead must be moved into the middle of the detection laser beam. For this purpose magnetic rotary encoders (EM20B-40, Alps, Appendix E), that output quadrature signals, were used. The quadrature signal is decoded with the FPGA-card and the resulting frequency control is output to the DIO ports. The LabVIEW program is shown in Figure 11.

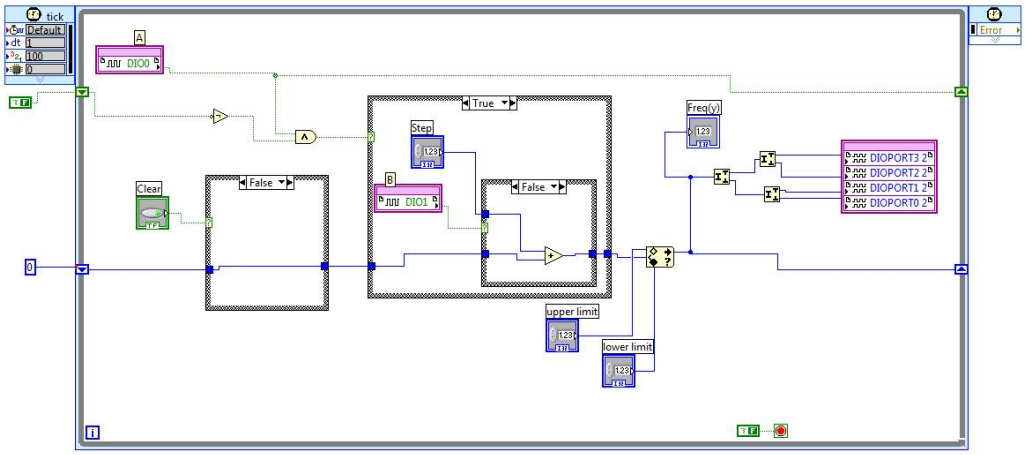


**Figure 11. Program to decode the quadrature signal from the magnetic encoders. The signal comes in (DIO0-1) and defines the direction of the step in the frequency output.**

## 3.7 Trapping experiment

A trapping chamber was made out of a microscope cover glass (0.17 mm thickness, Corning) and a microscope slide (2 mm thickness, Menzel-Gläser). In a two-sided tape (0.15 mm thick) a slit was cut and the glasses were stuck together to form a chamber. On one of the glasses PEEK tubes (1/16 inch outer diameter, 0.25 mm inner diameter, Upchurch Scientific) were connected from which the chamber could be filled (Figure 12). A mixture of water and 1 μm silica microspheres (Sicastar 1 μm, Micromod) were poured into the chamber in 1000:1 dilution. Trapping was started by opening the trapping laser shutter and steering the laser beam close to a microsphere. From the video image it was confirmed that only one bead was trapped. The bead was moved to the center of the detection laser and data collection was started. Time series with different feedback gains were then measured.

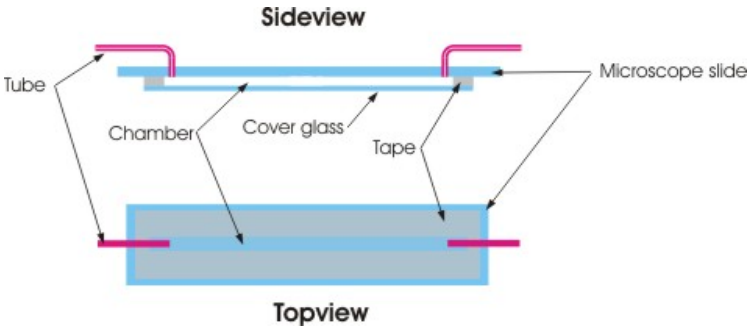


**Figure 12. Sample chamber made out of microscope cover glass and microscope slide.**

## 3.8 Data-analysis for the power spectra

To determine the power spectra of a bead's thermal motion, the bead position was measured. Using this data the power spectrum was calculated using the **pwelch** function in Matlab® with number of windows $n_w = 1$. This power spectrum is then compressed by blocking $n_b = 150$ consecutive data points. Blocking was done to make the exponentially distributed power spectrum values Gaussian distributed[23]. Fitting was then done to the blocked power spectrum $S^{(\exp)}$ using Eq.20 (±10 aliasing terms are considered) and minimizing the squared error[23]

$$\chi^2 = n_w n_b \sum \left( \frac{S^{(\exp)}}{S} - 1 \right)^2 . \qquad (23)$$

First the fitting was done for the data where there is no feedback control. From this fit parameters $D$ and $\frac{k}{\beta}$ were inferred. Next, holding these parameters constant, a fit to the data where the gain was highest was done. From this fit the delay parameter $\tau$ was inferred and subsequently held constant. Finally the rest of the data was fit to get all the gain constants $K_p$. Confidence intervals for fitting parameters were inferred by checking the $\chi^2{}_{\min} + 1$ values for each parameter[34].

# 4 Results

First, the AOD deflection efficiency was measured. Second, trap steering and time sharing was demonstrated. Third, the steering and position detection were calibrated. Finally, the position-clamp, using real-time feedback control, was tested.

## 4.1 AOD diffraction efficiency

The AOD deflection efficiency is highest when the incoming beam is at the Bragg angle (Eq. 7). However, this also sets the driving frequency $f_{AOD}$. When the beam is steered by changing the frequency also the Bragg angle changes and the deflection efficiency is no longer optimal. The deflection efficiency was measured scanning through the whole frequency band and measuring the laser power after the AODs with a laser power meter (Ophir Optics Ltd.). The results are shown in Figure 13.

Since the trap stiffness is proportional to the laser intensity, any intensity variation due to variable AOD diffraction efficiency causes a variable trap stiffness. For large trap movements (Figure 13A and D) this effect must be corrected for. However, in typical single-molecule experiments performed over short distances (1 μm) the trap stiffness variation is below 3 % (Figure 13C and F). This variation can usually be neglected, since calibration errors are of the same size.

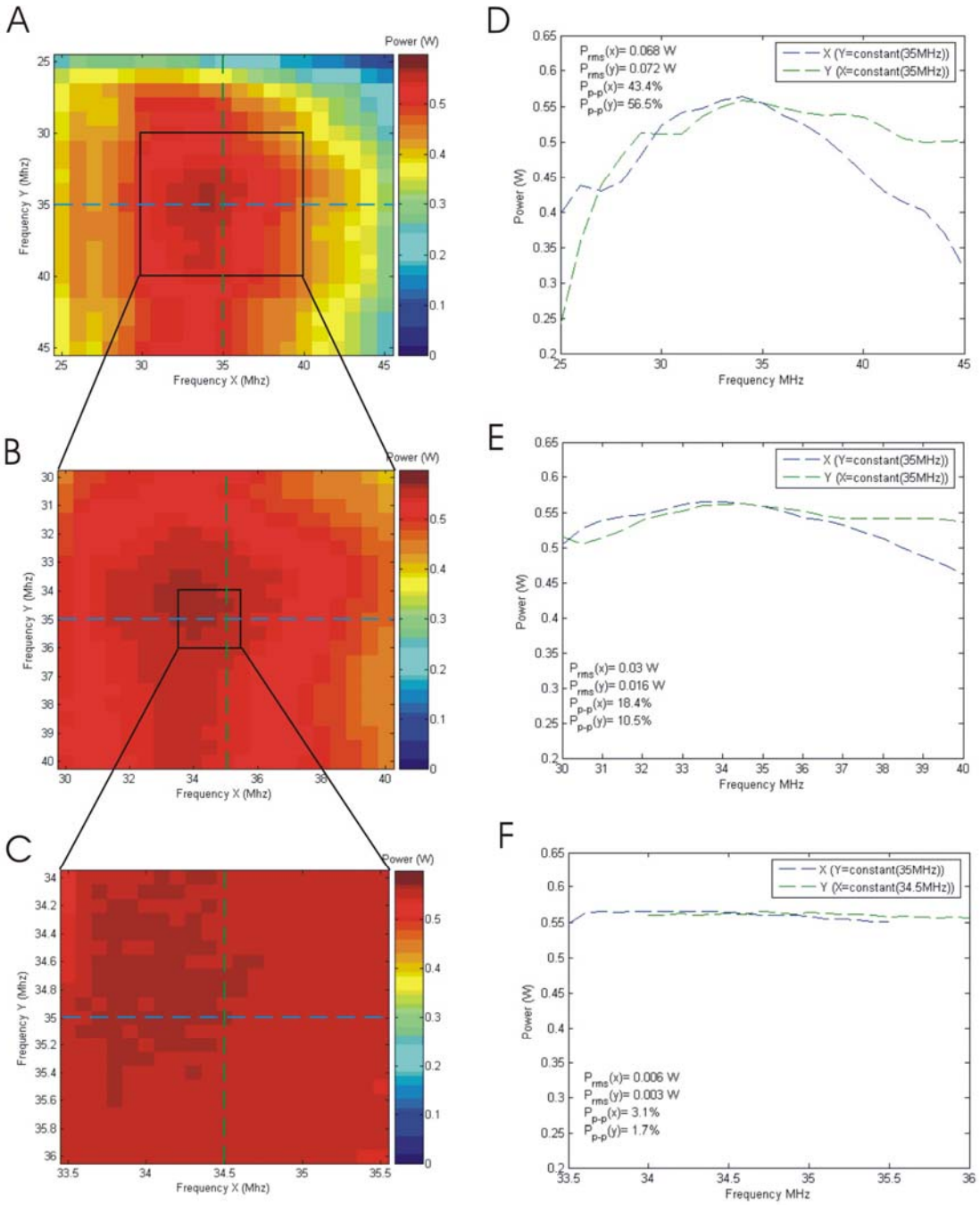


**Figure 13. Deflected laser power from the AODs, where the intensity drop due to the changed driving frequency $f_{AOD}$ can be seen. Due to slight misalignment of the AOD crystals the maximum diffraction efficiency is slightly displaced from the X/Y center frequency. The initial laser power was set to 1.35 W. Left: measured power after the AODs for different X and Y frequencies. The frequencies along each axis correspond to 11 µm, 5 µm and 1 µm (A, B and C) trap movement in the focal plane. The dashed lines in the left figures indicate intensity profiles shown on the right. The calculated corresponding rms variation (in W) and peak-to-peak value (in %) are also shown.**

## 4.2 Steering

Steering capabilities were tested by moving four time shared traps in a circle. In each time-shared trap an individual 1 µm bead was trapped. Figure 14 shows four images with 0.2 s intervals. Individual traps are 'on' for 12.5 µs (500 periods at 40 MHz clock

rate) and 'off' for 37.5 μs (3×500 periods). The traps are then moved in a circle counter-clockwise.

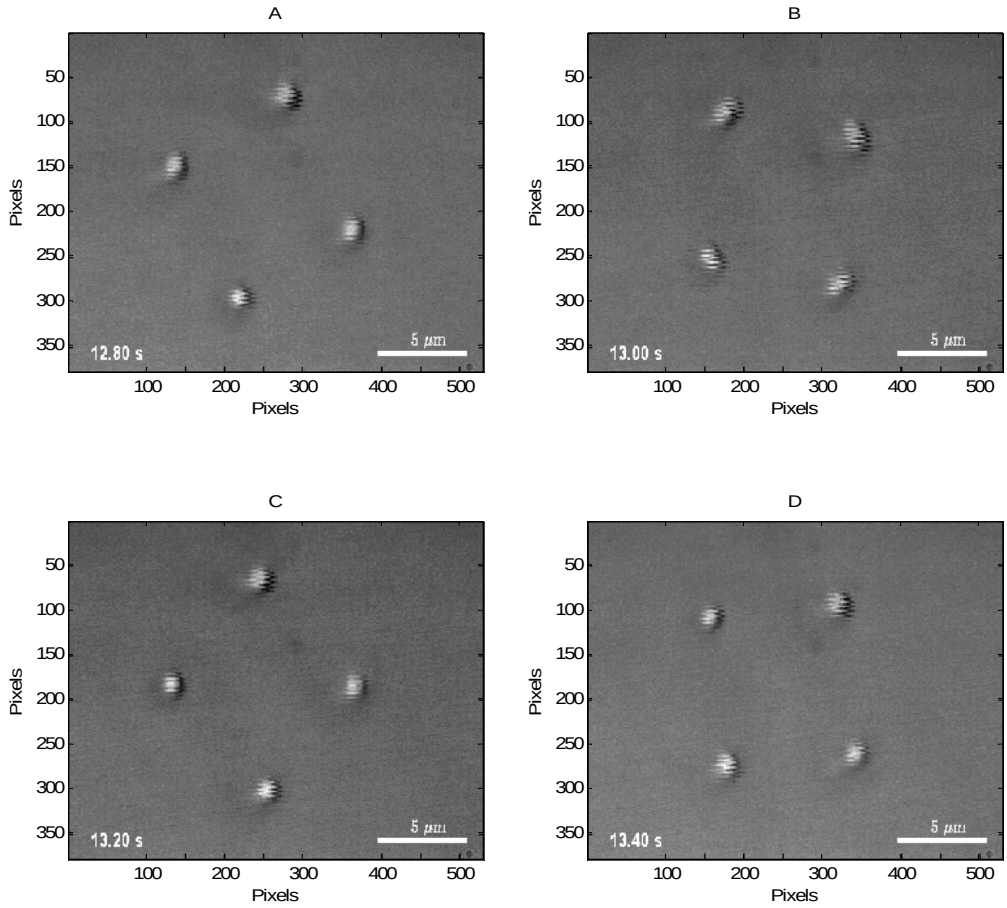


**Figure 14. Four time shared traps moved counter-clockwise. Frames from A to D are taken with 0.2 s intervals. The full video is available at[35]**

## 4.3 Calibrations

Results from the AOD position calibration and PSD calibration are presented. First the pixels of the video image are calibrated with a micrometer ruler. Then the AODs are calibrated by particle tracking and finally the position sensitive detector (PSD) is calibrated.

### 4.3.1 Video Image

The pixels of the video image were calibrated with a 0.1 mm micrometer scale (S12-Stage micrometer, Pyser-SGI) with 0.002 mm divisions. An image of this ruler is shown in Figure 15. With a tube-lens magnification of 1.5 the correspondence between pixels and distance in the focal (specimen) plane was 44.2±0.2 nm/pixel. Errors are estimated visually from Figure 15.

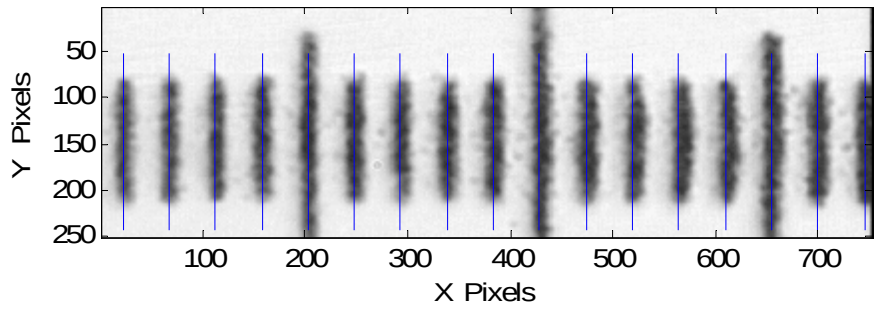


**Figure 15. An image of the micrometer scale with 2 µm divisions. Vertical lines (blue) added with Matlab. From this image one can deduce the correspondence between the pixel index and distance in the specimen plane. One pixel in the CCD-camera corresponds to 44.2 nm.**

### 4.3.2 AOD calibration

After the CCD-camera was calibrated, a 1 µm trapped bead was scanned through the range of the AOD. Pictures were taken after each AOD 1 MHz frequency step. One of these video images is shown in Figure 16A. Digitization noise was removed by convolving the image with a Gaussian surface (Figure 16A inset). Figure 16B shows all the images after the convolution. Using the brightest pixel the geometric center of the trapped bead was tracked from each image (Section 2.4.1).

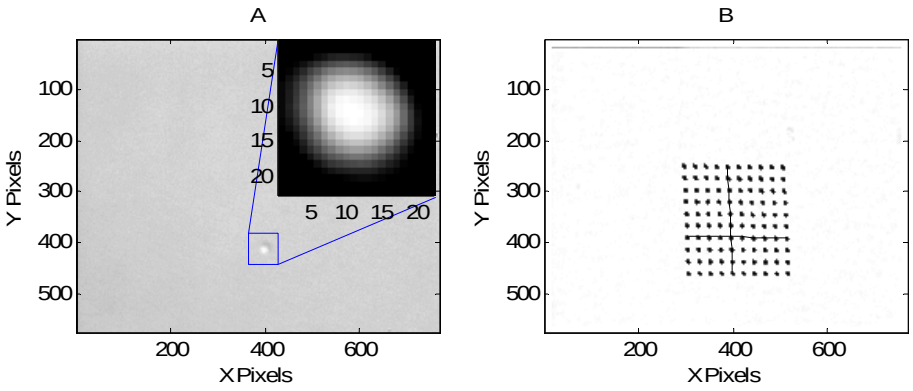


**Figure 16. A) Video image of a 1 µm trapped bead and magnified bead image after convolution (Eq.9). From this image the geometric center (Eq.10) is deduced. B) All images after the convolution (colors changed for imaging purposes). From this scan the correspondence between the AOD frequency and trap position can be inferred. Black lines show where the points in Figure 17 are taken.**

In Figure 17A the bead is moved in the X-direction and the resulting bead positions are calculated in pixels. The correspondence between AOD frequency and the position was established to be 23.21±0.03 pixels/MHz, which means that the AOD position calibration constant is $\alpha = 1.026 \pm 0.001$ µm/MHz (Eq.8). In Y-direction the correspondence was 23.21±0.04 pixels/MHz, Figure 17B. Errors are fitting errors.

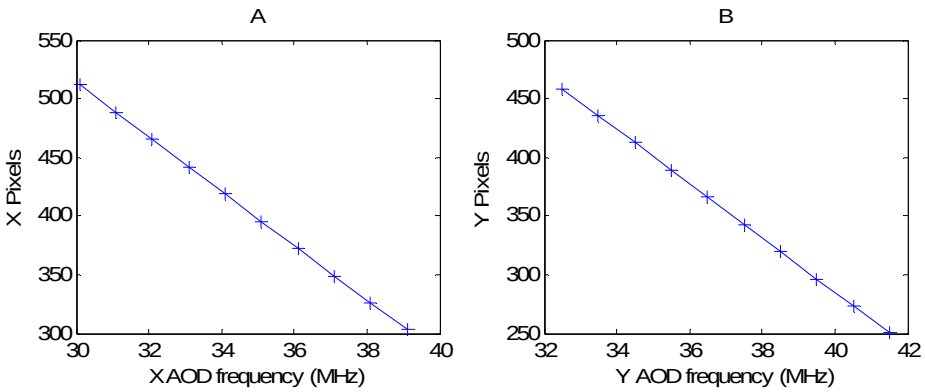


**Figure 17. The tracked particle positions in pixels as a function of AOD frequency. A) Scan along the X-axis. The frequency in the Y-direction was kept constant at 35.5 MHz. B) Scan along the Y-axis. The frequency in the X-direction was kept constant at 35.1 MHz.**

### 4.3.3 PSD calibration

A 1 µm bead trapped using 0.5 W laser power was moved in an 11x11 raster scan and at each position 3018 voltage measurements were averaged (100 ms data collection at 50 kS/s and 1/5 of data at the beginning and at the end not used). Signals from the detectors are shown as surface plots in Figure 18. Equation 11 ($n=1$) was fit to this data to get the calibration parameters shown in Table 1.

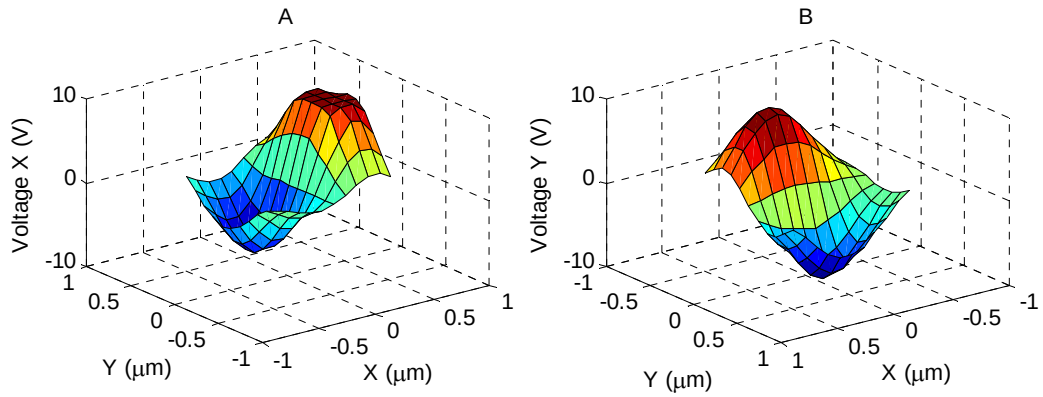


**Figure 18. Voltage signals from the PSD. (A) shows the X-signal and (B) shows the Y-signal. X and Y axes are the bead positions in µm and the Z-axis shows the voltage signal in volts. In (A) the signal is cut above 10 volts.**

Figure 19 shows a contour plot of the measured voltages. Also shown is the region where the fit was made. In this region there are 12 points.

**Table 1. Parameters for Eq.11 resulting from a fit to the data shown in Figure 18**

| | $b_{00}$ (nm) | $b_{01}$ (nm/V) | $b_{10}$ (nm/V) | $b_{11}$ (nm/V$^2$) |
|---|---|---|---|---|
| X | -25.0±1.2 | 0.38±0.06 | 22.0±0.3 | -0.33±0.05 |
| Y | 23.6±1.3 | -26.4±0.4 | -0.09±0.04 | 0.10±0.04 |

The parameter $b_{10}$=22.0±0.3 nm/V gives the sensitivity for position detection along the X-axis. The sensitivity for position detection along the Y-axis is $b_{01}$=26.4±0.4 nm/V. Using the parameters in Table 1, the RMS error between the fit and the data was 7.8 nm

for X and 10.6 nm for Y. If the parameter $n$ in Eq. 11 is increased to 2, the RMS errors for X and Y are 7.3 nm and 3.7 nm respectively.

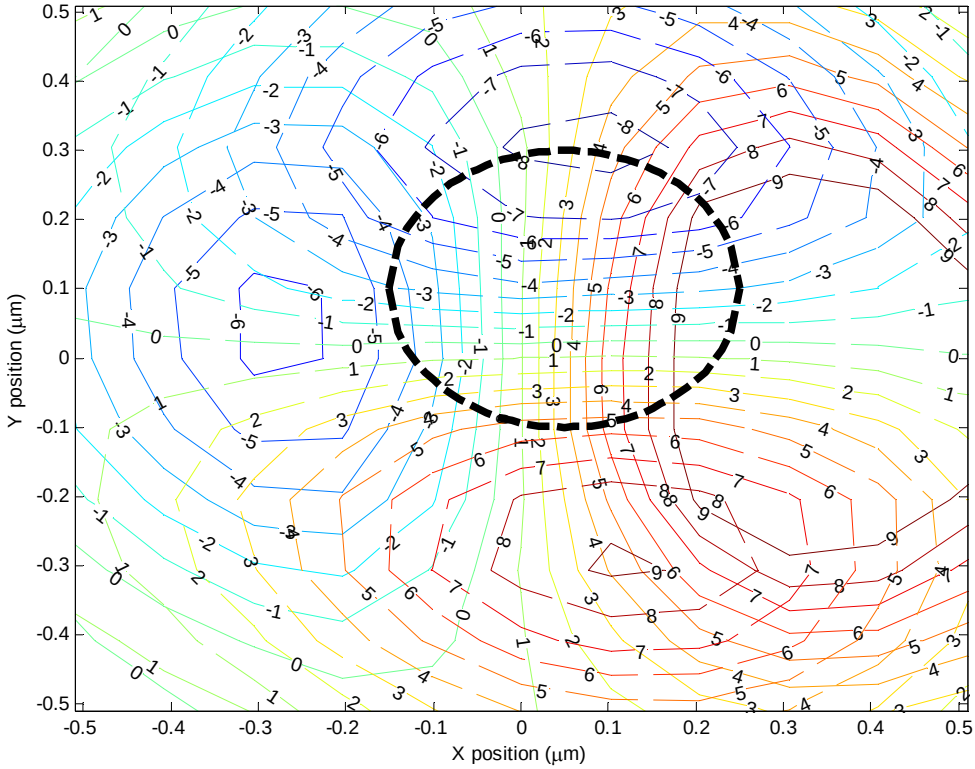


**Figure 19. Contour plot showing constant-voltage lines from a measurement using an 11x11 raster scan. Solid colored lines show the X-axis voltage. Dashed colored lines show the Y-axis voltage. Dashed black line shows the region where the fit was made to get the parameters of Table 1. In this region there is a one to one correspondence between X and Y voltages and bead position. Inside this region bead position can be tracked with nanometer resolution.**

## 4.4 Position clamp feedback control

The control algorithm implemented on the FPGA-card was a simple proportional feedback control. The position signal from the sensor is a voltage that is digitized with 16-bit resolution. After calibration a 1 V signal corresponds to 22.0 nm bead movement. The resulting 16 bit number is multiplied with an integer corresponding to the feedback gain. The result is then used for steering. The DDS modifies the 32 bit number to a RF-signal where a 1 MHz change in frequency corresponds to a 1.026 µm change in trap position in the specimen plane. For example setting G=100 corresponds to a dimension-less gain of (see Eq.14)

$$K_p = \left(\frac{1}{0.0220}\frac{2^{15}}{10}\right)(100)\left(\frac{1000}{2^{31}}\right)(1.026) = 7.1. \qquad (24)$$

In Figure 20, using $K_p = 7.1$, it can be seen that the trap position follows exactly the motion of the bead, inverted and with ca 7-times bigger amplitude. The position of the trap was calculated from the control word written into the DDS.

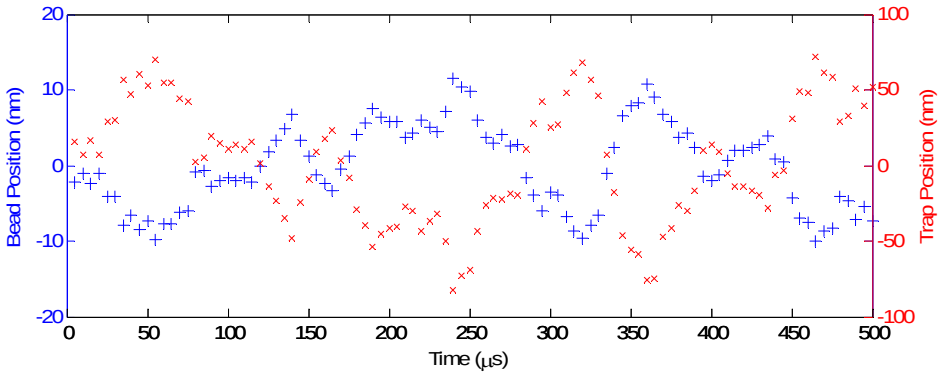


**Figure 20. Position of the trapped bead (left y-axis, blue +) and the corresponding position of the trap (right y-axis, red x) as a function of time with $K_p = 7.1$. Data points are with 5 μs intervals corresponding to 200 kS/s sampling frequency. This data verifies that the feedback control works as designed, the trap position constantly following, inverted and 7-fold amplified, the bead position.**

Feedback control was tested with two trapping laser powers (500 mW and 100 mW) for five different gain settings ($K_p$ = 0, 7.1, 14.2, 21.3 and 28.4). A bead of 1 μm diameter was trapped and moved to the detection beam center ($x_{set} = 0$, Figure 5). The feedback was then turned on and the bead position was measured with different gain parameters for 1.4 s with a trap laser power of 500 mW. When the power was 100 mW the data was measured for 1.6 s. Both the position of the bead and the trap are shown in Figure 21. The gains (G in Figure 10) were 0, 100, 200, 300 and 400. According to eq.24 these correspond to $K_p$ gains of 0, 7.1, 14.2, 21.3 and 28.4. Trapping became unstable (Figure 25) with a trapping laser power of 100 mW and gains of $K_p > 14$, preventing measurements of the time-series for $K_p = 21.3$ and $K_p = 28.4$.

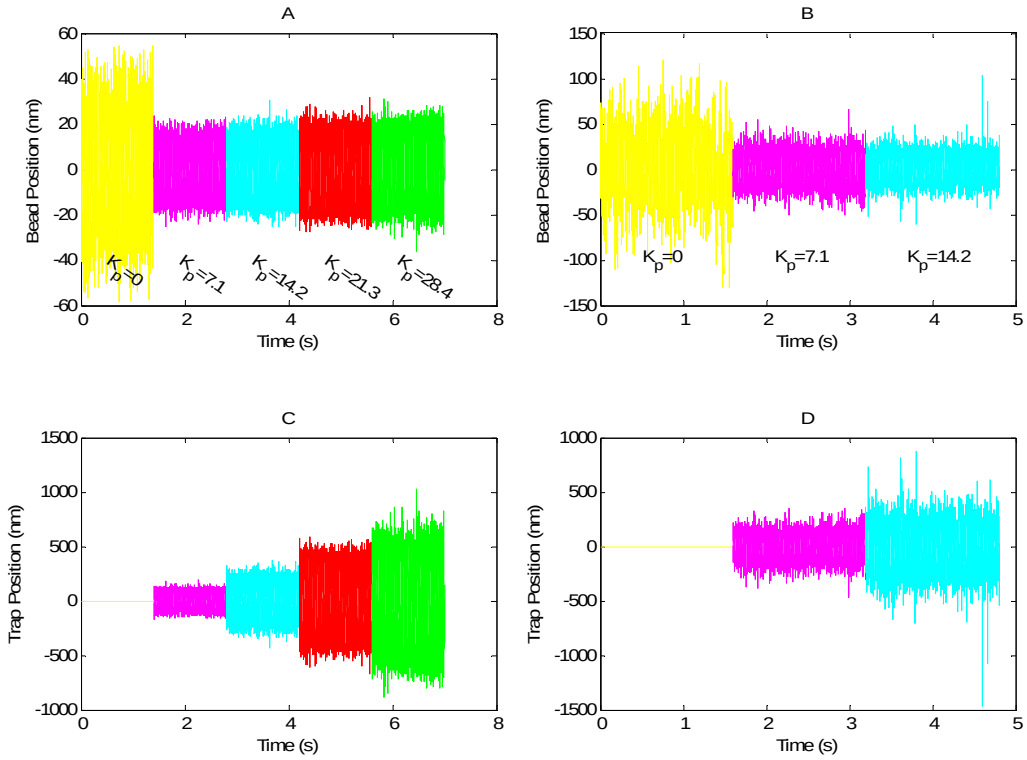


**Figure 21. (A) Position of the trapped bead with five different gains 0, 7.1, 14.2, 21.3 and 28.4. The laser power was 500 mW. (B) Position of the trapped bead with three different gains 0, 7.1 and 14.2. The laser power was 100 mW. (C) Position of the trap corresponding to the data in part A. Colors as in (A). (D) Position of the trap corresponding to the data in B Colors as in (B).**

The power spectral density was then calculated as explained in section 3.8, and Eq.20 was fit to the power spectral density. The resulting parameter values are shown in Appendix D. The power spectra and the resulting fits are shown in Figure 22 and Figure 23.

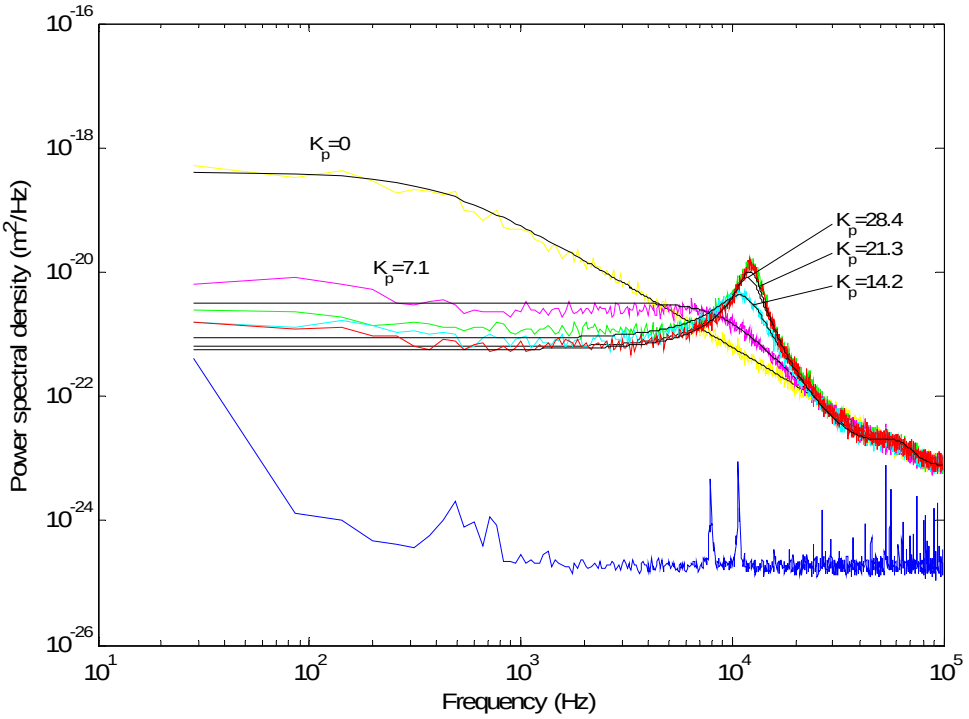


**Figure 22. Power spectra of the bead position and fits to data (Eq.20). Colors of the traces are the same as in Figure 21. A bright noise spectrum (same measurement, but without a trapped bead) is also shown (blue trace). Laser power was 500 mW. Data at $K_p > 0$ clearly shows the reduced power spectral density at frequencies up to 10 kHz.**

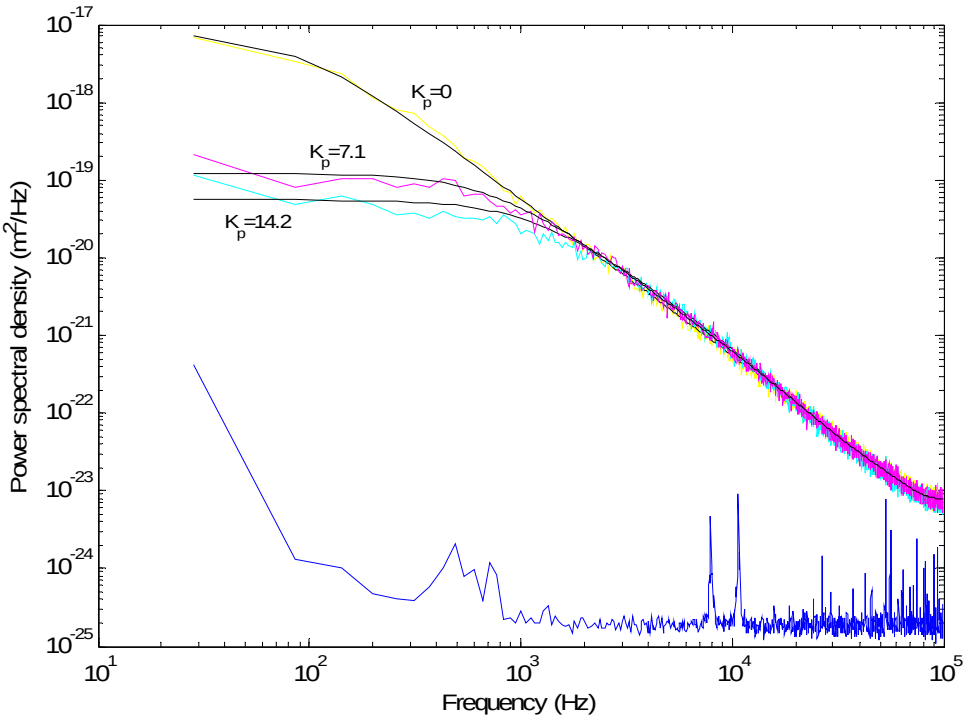


**Figure 23. Power spectra of the bead position and fits to data (Eq.20). Colors of the traces are the same as in Figure 21. A bright noise spectrum (same measurement, but without a trapped bead) is also shown (blue trace). Laser power was 100 mW. In contrast to Figure 22 the power spectra at $K_p = 7.1$ and $K_p = 14.2$ remain roughly Lorentzian.**

The variance of the trap with different gains was calculated using Eq.21, cfr. Figure 22 and Figure 23. The variances are shown in Figure 24. When the feedback gain $K_p$ was increased from 0 to 7.1 the effective stiffness increased to 7.2-fold (laser power 500 mW). For 100 mW laser power, when the gain $K_p$ was raised to 14.2, the stiffness became 12.1 times larger than without the gain.

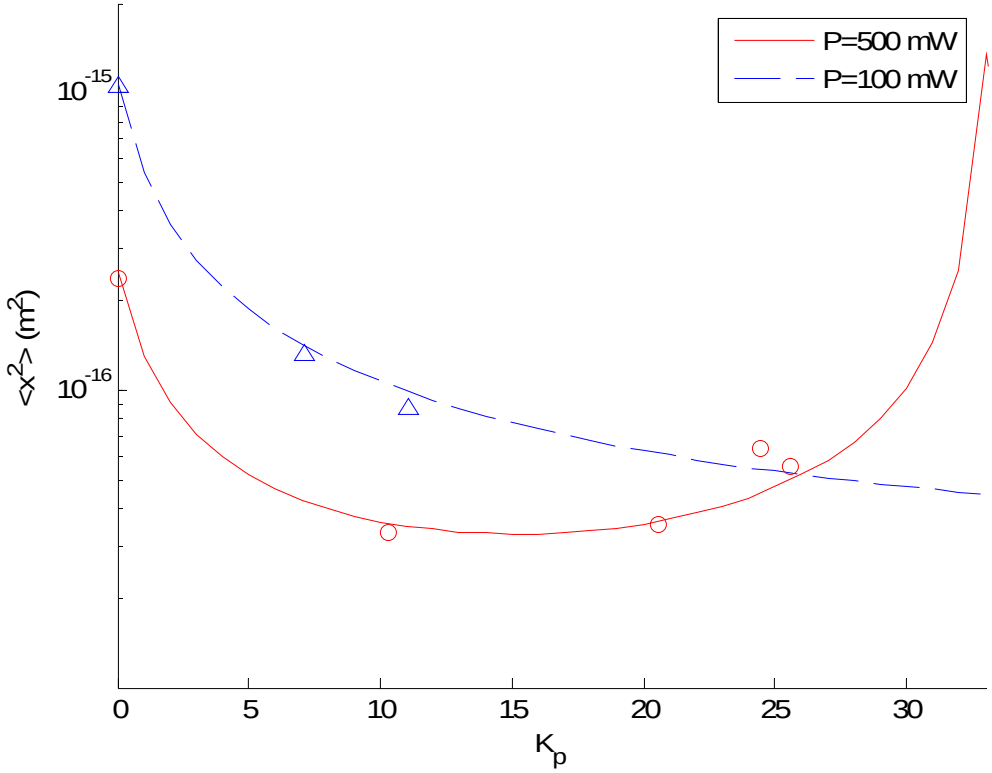


**Figure 24. Variance $\langle x^2 \rangle$ as a function of proportional gain. Lines are calculated by numerical integration using Eqs.20 and 21 and the fitted parameters. Solid red line is with 500 mW laser power whereas the dashed blue line is for the case where the power was 100 mW. Red circles and blue triangles are calculated from the measured power spectra using Eq.21. Experimental data agrees well with theory, and indicates that an optimal feedback gain exists where the variance is at minimum (i.e. the effective trap stiffness is maximized).**

If the gain is increased too much the trapping becomes unstable. Already when the laser power was 500 mW and the gain $K_p$ was 28.4 there were sometimes spikes when the trap jumped from one place to another. Data from this kind of unstable trapping is shown in Figure 25.

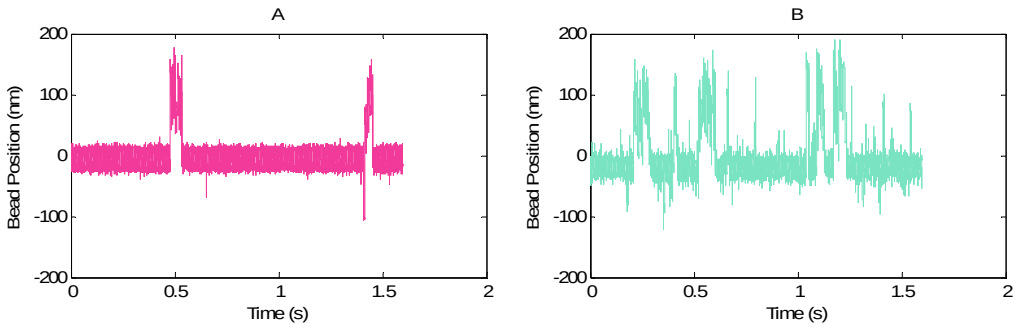


**Figure 25. Position of the trapped bead as a function of time. Unstable trapping can be seen as large random deviations in bead position. (A) Laser power 500 mW and $K_p = 28.4$. (B) Laser power 100 mW and $K_p = 21.3$.**

# 5 Discussion

Using optical tweezers in position clamp feedback control it was possible to decrease the variation in position of 1 μm silica microspheres by a factor of 12.1. The effective stiffness was thus 12.1 times larger than without control (100 mW trap laser power). For 500 mW trap laser power the stiffness increased to 7.2-fold. In comparison to the result of Simmons *et. al* [8] (400-fold decrease in position variance) these are much lower values. However, their results have not been reproduced.

The data shows a resonance peak building up when the feedback gain is increased. The theory shows that this is caused by the delays in the feedback loop. The fits to the data gives a delay $\tau$ of about 20 μs (Table 5, Appendix D). The AD-conversion and the AOD access time are the major sources of delay in the feedback loop. The analog signal is digitized at 200 kS/s. This gives a 5 μs delay. In steering there is also an AOD delay, corresponding to the time that it takes for the sound wave to travel through the AOD (about 5 μs). The calculations in the FPGA-card are done at a 40 MHz rate, so the calculations of the control loop are done in a few hundred nanoseconds. The direct digital synthesizer takes 40 ns to settle to a new frequency. These delays account for about 10 μs, only half of the delay found by fitting to the data.

Fits to the data resulted in gain factors of $K_p$ = 10.27±0.05, 20.54±0.05, 25.59±0.03 and 24.46±0.02 for a laser power of 500 mW (Table 6, Appendix D). The actual gain factors used were 7.1, 14.2, 21.3 and 28.4 (see Eq. 24). Thus the fit $K_p$ deviates from the used $K_p$ factors found by calibration, but the increasing tendency of the fit parameters is correct. Only for the last dataset ($K_p$=28.4) the fit resulted in a smaller fit gain, but in this data set trapping became unstable. With 100 mW laser power the fit resulted in gains of 7.14±0.10 and 11.08±0.13, which correspond roughly to the used gains of 7.1 and 14.2.

Optical trapping theory usually doesn't take into account that the trap doesn't stay harmonic to infinity. When control is too violent and the trapping laser is moved too far the bead doesn't feel the trap anymore. This causes unstable trapping. Unstable trapping may lead to increased variance with increasing gain. Another error source is the detection laser. If there are disturbances in the detection laser the feedback would try to compensate these errors. As a result the variance of the bead position would increase but this wouldn't be detected. This kind of behavior could be verified by using another detection laser and a position detector which is not part of the feedback loop.

A small position variance means that position clamp feedback control can be used to achieve better spatial control of trapped particles than without feedback control. The position clamp is also useful when low trap laser powers must be used. Heating of the solution become important for laser powers exceeding 100 mW [12]. When small particles are trapped heating effects are even more important. Trapped gold nanoparticles display a temperature increase of 20 K when the laser power is increased by 100 mW[36]. Thus the developed real-time position clamp is useful when stiff trapping of small 'hard-to-trap' particles is desired, but the maximum laser power must be limited.

Force clamp mode, where feedback control keeps the force acting on a trapped particle constant, is used when molecular motors are measured[37]. Motor properties should be measured under constant load so as not to disturb the motor function. This kind of force

clamp mode can easily be adapted to the instrument presented in this work. The high degree of freedom in programming of the FPGA-card makes it possible to use different controlling algorithms. A next step could be to introduce the rest (integral and derivative parts) of a conventional Proportioanl Integral Derivative-controller.

# 6 Conclusion

An optical tweezers instrument capable of real-time position clamp feedback control was constructed. Proportional control reduced the bead position variance. An effective trap stiffness 12.1-times stronger than without feedback control was achieved.

# 7 References


1. Svoboda, K. and S.M. Block, *Biological applications of optical forces.* Annu Rev Biophys Biomol Struct, 1994. **23**: p. 247-85.
2. Neuman, K.C. and S.M. Block, *Optical trapping.* Review of Scientific Instruments, 2004. **75**(9): p. 2787-2809.
3. Greenleaf, W.J., M.T. Woodside, and S.M. Block, *High-Resolution, Single-Molecule Measurements of Biomolecular Motion.* Annu Rev Biophys Biomol Struct, 2007.
4. Ritort, F., *Single-molecule experiments in biological physics: methods and applications.* J. Phys.: Condens. Matter, 2006. **18**: p. R531-R583.
5. Bustamante, C., J.C. Macosko, and G.J.L. Wuite, *Grabbing the cat by the tail: manipulating molecules one by one.* Nat. Rev. Mol. Cell Biol, 2000. **1**: p. 130-136.
6. Kodera, N., M. Sakashita, and T. Ando, *Dynamic proportional-integral-differential controller for high-speed atomic force microscopy.* Review of Scientific Instruments, 2006. **77**: p. 083704.
7. Ashkin, A. and J.M. Dziedzic, *Feedback stabilization of optically levitated particles.* Applied Physics Letters, 1977. **30**: p. 202.
8. Simmons, R.M., et al., *Quantitative measurements of force and displacement using an optical trap.* Biophysical Journal, 1996. **70**(4): p. 1813-1822.
9. Ranaweera, A., *Investigations with Optical Tweezers: Construction, Identification, and Control*. 2004, UNIVERSITY OF CALIFORNIA.
10. Wulff, K.D., D.G. Cole, and R.L. Clark, *Servo control of an optical trap.* Applied Optics, 2007. **46**(22): p. 4923-4931.
11. Pilizota, T., et al., *A Programmable Optical Angle Clamp for Rotary Molecular Motors.* Biophysical Journal, 2007. **93**(1): p. 264.
12. Peterman, E.J.G., F. Gittes, and C.F. Schmidt, *Laser-Induced Heating in Optical Traps.* Biophysical Journal, 2003. **84**(2): p. 1308-1316.
13. Atarah, S., *Construction and Calibration of a Versatile Optical Trap For Studying Molecular Motors*, in *Department of Physics and Department of Biosciences*. 2001, University of Helsinki: Helsinki.
14. Ojala, H., et al. *Stiffer Optical Tweezers With Feedback Control*. in *41th Physics Days of the Finnish Physical Society*. 2007. Tallinn, Estonia.
15. Gittes, F. and C.F. Schmidt, *Interference model for back-focal-plane displacement detection in optical tweezers.* Opt. Lett, 1998. **23**(1): p. 7-9.
16. http://sine.ni.com/cs/app/doc/p/id/cs-802.
17. Allersma, M.W., et al., *Two-Dimensional Tracking of ncd Motility by Back Focal Plane Interferometry.* Biophysical Journal, 1998. **74**(2): p. 1074-1085.
18. Hecht, E., *Optics*. 2002, San Francisco: Addison Wesley.

19. Mäkynen, A., *Position-sensitive devices and sensor systems for optical tracking and displacement sensing applications*. 2000: Oulun yliopisto.

20. Dixon, R., *Acoustic diffraction of light in anisotropic media.* Quantum Electronics, IEEE Journal of, 1967. **3**(2): p. 85-93.

21. Chang, I.C., *I. Acoustooptic Devices and Applications.* Sonics and Ultrasonics, IEEE Transactions on, 1976. **23**(1): p. 2-21.

22. Crocker, J.C. and D.G. Grier, *Methods of digital video microscopy for colloidal studies.* J. Colloid Interface Sci, 1996. **179**(1): p. 298-310.

23. Berg-Soerensen, K., *Power spectrum analysis for optical tweezers.* Review of Scientific Instruments, 2004. **75**(3): p. 594.

24. Gosse, C. and V. Croquette, *Magnetic Tweezers: Micromanipulation and Force Measurement at the Molecular Level.* Biophysical Journal, 2002. **82**(6): p. 3314-3329.

25. Berg-Soerensen, K., *Unintended filtering in a typical photodiode detection system for optical tweezers.* Journal of Applied Physics, 2003. **93**(6): p. 3167.

26. Huisstede, J.H.G., et al., *Dependence of silicon position-detector bandwidth on wavelength, power, and bias.* Optics Letters, 2006. **31**(5): p. 610-612.

27. Uchida, N. and Y. Ohmachi, *Elastic and Photoelastic Properties of TeO Single Crystal.* Journal of Applied Physics, 1969. **40**(12): p. 4692.

28. Yano, T., et al., *TeO2 anisotropic Bragg light deflector without midband degeneracy.* Applied Physics Letters, 1975. **26**: p. 689.

29. *Operating Manual, 35 MHz Center Frequency Off Axis Acousto-optic Beam Deflector.* Neos Technologies, 2004.

30. Tocci, R.J., N.S. Widmer, and G.L. Moss, *Digital Systems; Principles and Applications*. 2007, New Jersey: Pearson Prentice Hall.

31. *NI 783xR User Manual.* National Instruments, 2005.

32. Floyd, T.L., *Digital Fundamentals*. 8 ed. 2003, New Jersey: Prentice Hall.

33. Visscher, K., S.P. Gross, and S.M. Block, *Construction of multiple-beam optical traps withnanometer-resolution position sensing.* Selected Topics in Quantum Electronics, IEEE Journal of, 1996. **2**(4): p. 1066-1076.

34. Bevington and Robinson, *Data Reduction and Error Analysis for the Physical Sciences*. 3 ed. 2003, New York: McGraw-Hill.

35. http://video.google.com/videoplay?docid=-4040903066530434288.

36. Seol, Y., A.E. Carpenter, and T.T. Perkins, *Gold nanoparticles: enhanced optical trapping and sensitivity coupled with significant heating.* Optics Letters, 2006. **31**(16): p. 2429-2431.

37. Wallin, A.E., A. Salmi, and R. Tuma, *Step Measurement - Theory and Simulation for Tethered Bead Constant-Force Single Molecule Assay.* Biophys. J., 2007: p. biophysj.106.097915.

# 8 Appendix

## A. Optical components

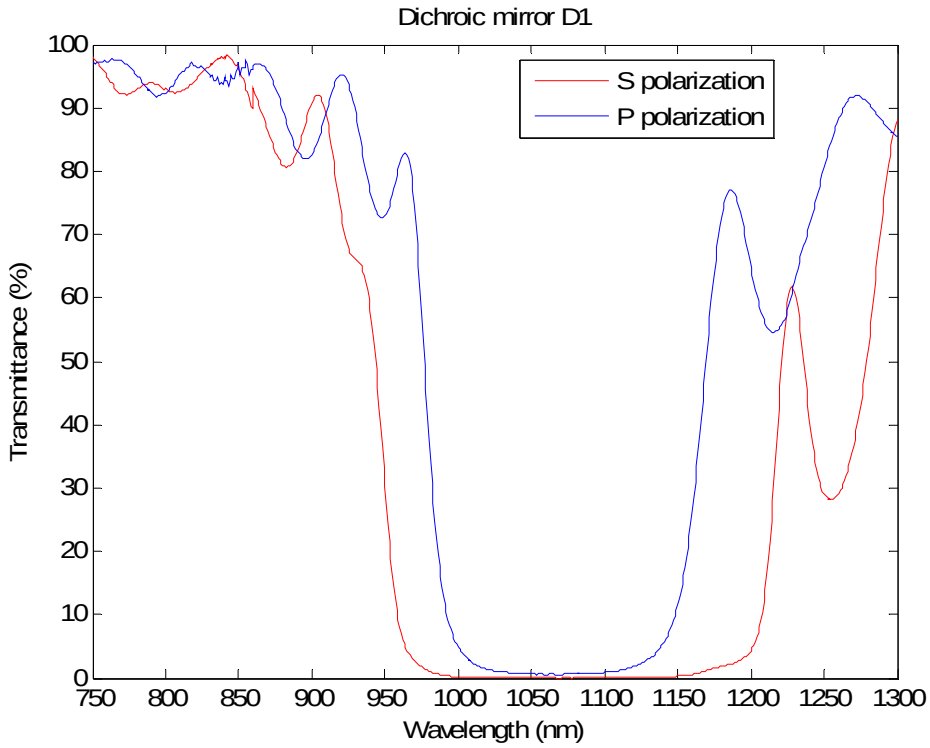


**Appendix Fig. 1. Transmission for the dichroic mirror D1, (SWP-45-RU1064-TU850-PW-2025-C, CVI Laser) which combines the trapping laser and the detection laser. The trapping laser (1064 nm) is reflected and the detection laser (830 nm) passes through.**

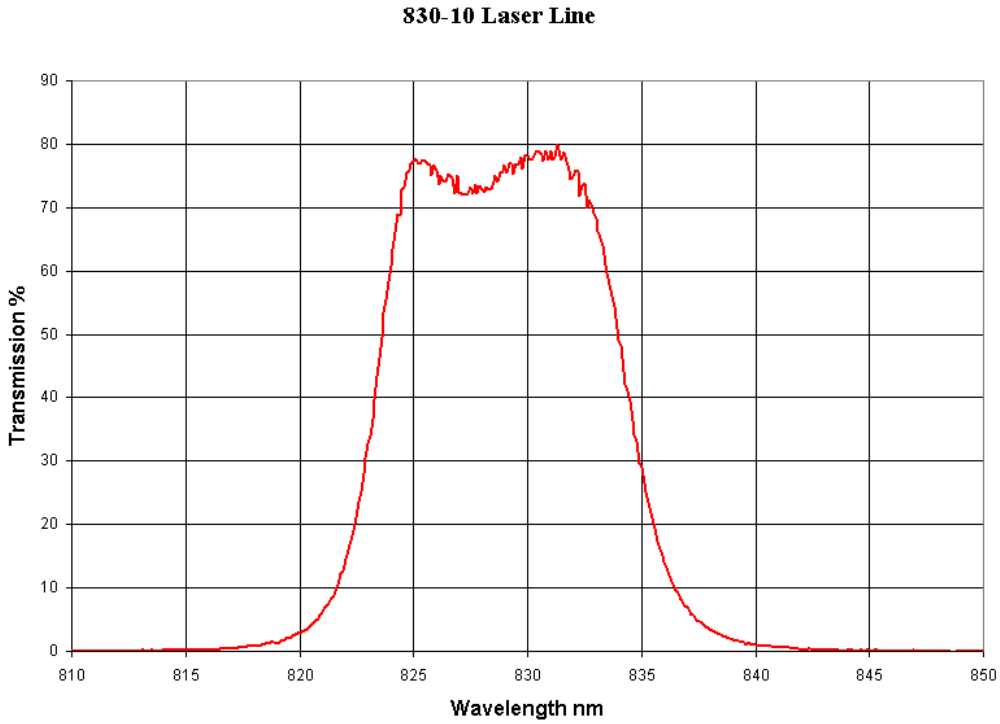


**Appendix Fig. 2. Transmission of the bandpass filter F1 (FL830-10, Thorlabs), which lets only the detection laser (830 nm) to reach the detector.**

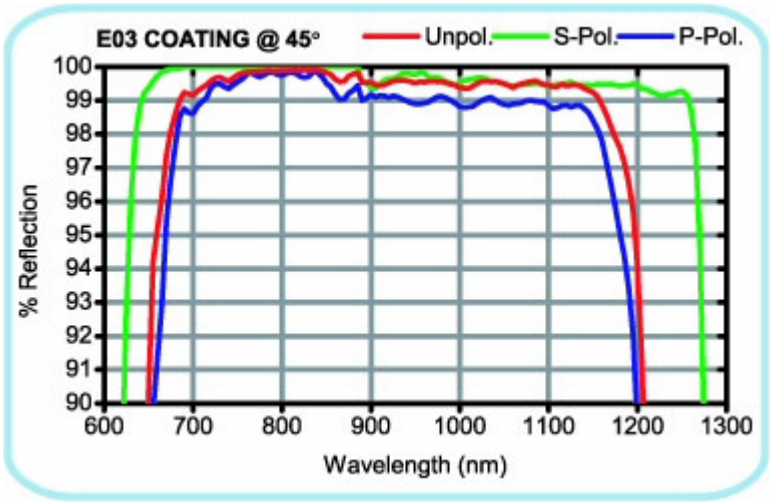


**Appendix Fig. 3. Reflection of broadband dielectric mirror D3, (BB2-E03, Thorlabs), which allows the visible light to go though the sample chamber to the video camera, but reflects the trapping laser (1064 nm) and the detection laser (830 nm).**

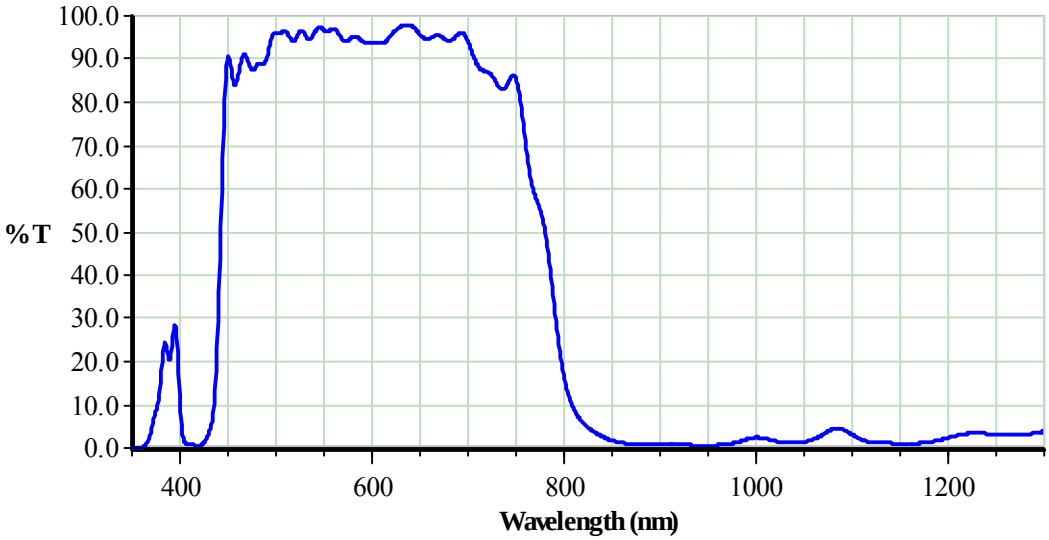


**Appendix Fig. 4. Transmission spectrum of dichroic mirror D2 (780dcspxr, Chroma), which reflects the trapping laser (1064 nm) and the detection laser (830 nm), but allows the visible light to reach the video camera.**

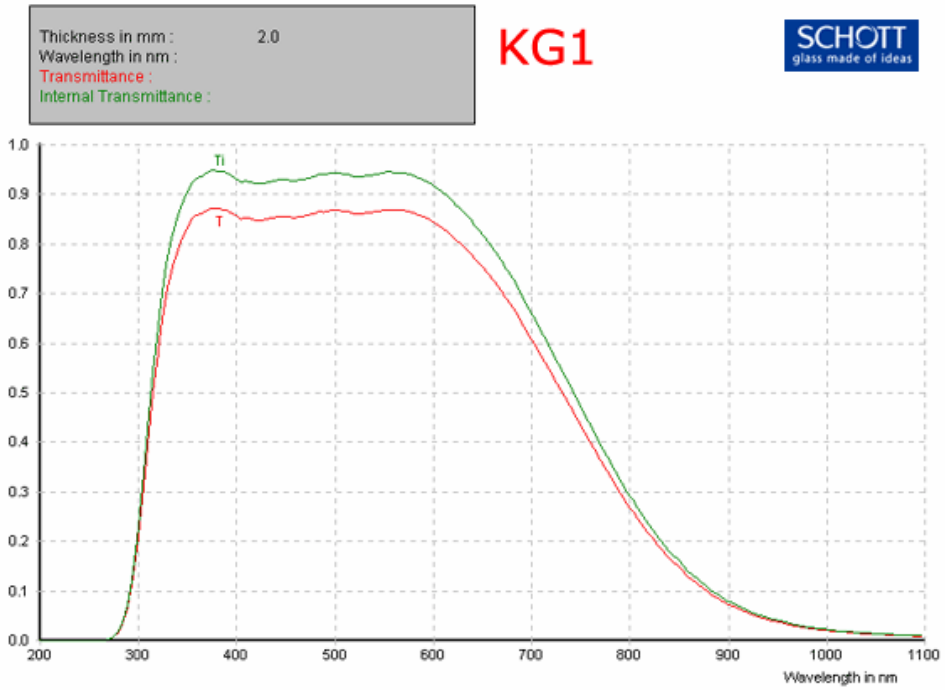


**Appendix Fig. 5. Transmittance for filter F2 (KG1) (can be exchanged with KG3, Appendix Fig. 6), which partly blocks the detection laser (830 nm) and the trapping laser (1064 nm), so that they can still be seen on the video screen. For wavelengths 850 and 1060 transmittances are 0.15 and 0.01, respectively.**


**Appendix Fig. 6. Transmittance for F2 (KG3) (can be exchanged with KG1, Appendix Fig. 5), which is used to totally block the trapping laser (1064 nm) and the detection laser (830 nm) from the video camera. For wavelengths 850 and 1060 transmittances are 0.04 and 0.0006, respectively.**

# B. Electronic circuits

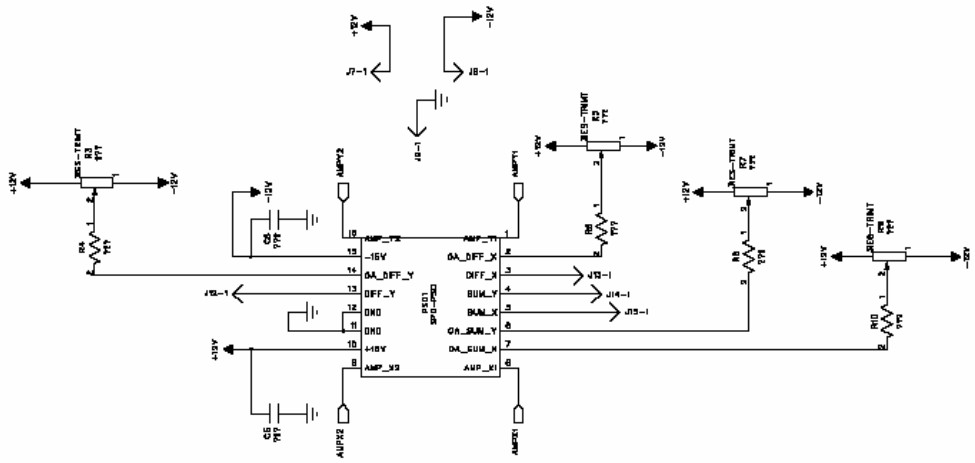

**Appendix Fig. 7. Schematics for PSD (S2-0171, Sitek).**

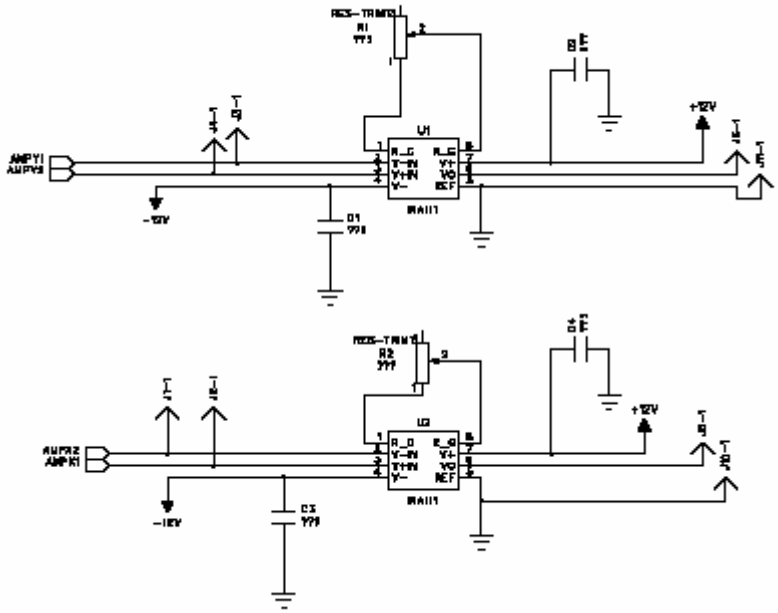

**Appendix Fig. 8. Schematics for instrumentation amplifiers (INA111) used in PSDs.**

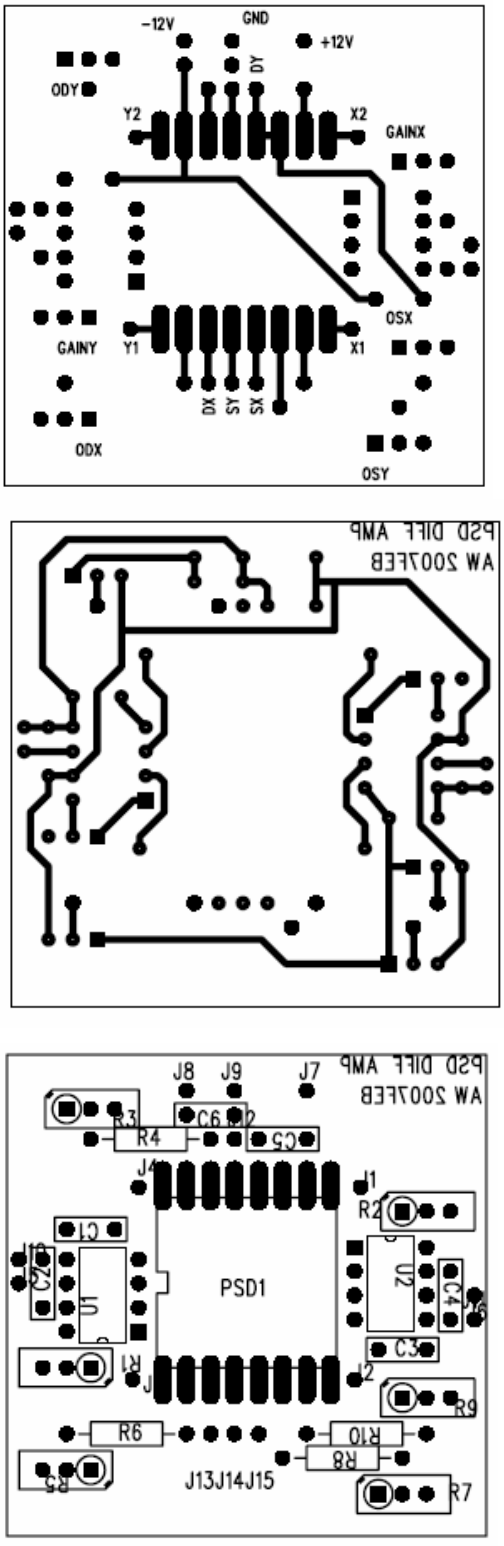


**Appendix Fig. 9. Circuit board for PSDs. Topside, solderside and assembly drawing. (5 cm × 5 cm).**

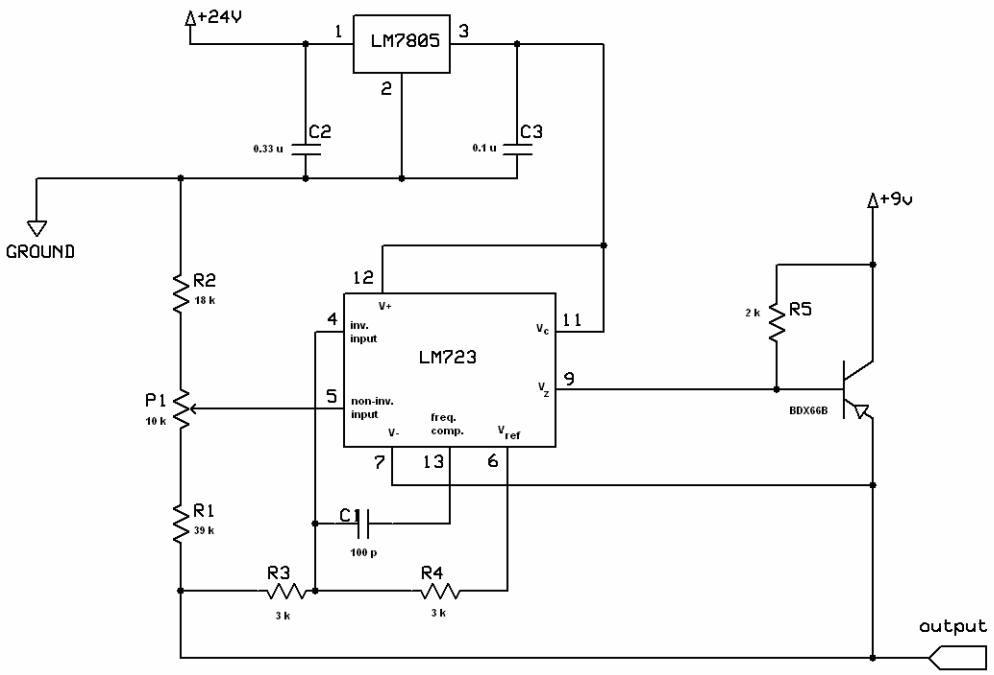


**Appendix Fig. 10. Schematics for the negative regulator LM723.**

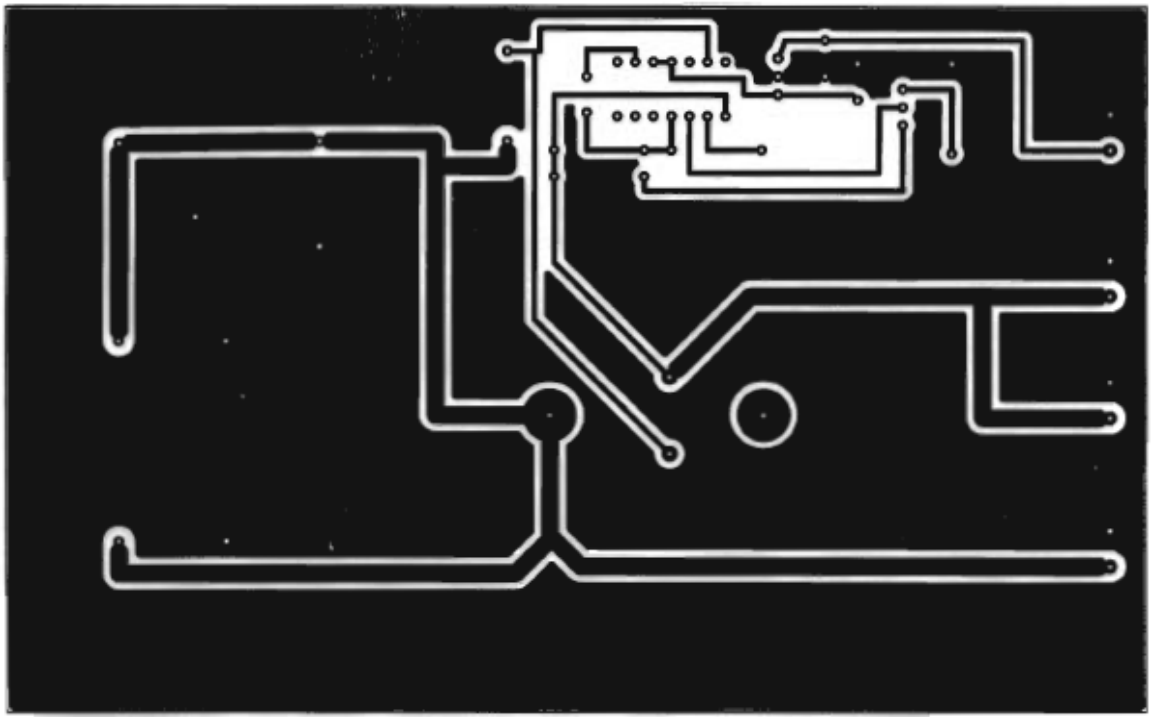

**Appendix Fig. 11. Circuit board for negative voltage regulator (10 cm × 16 cm)**

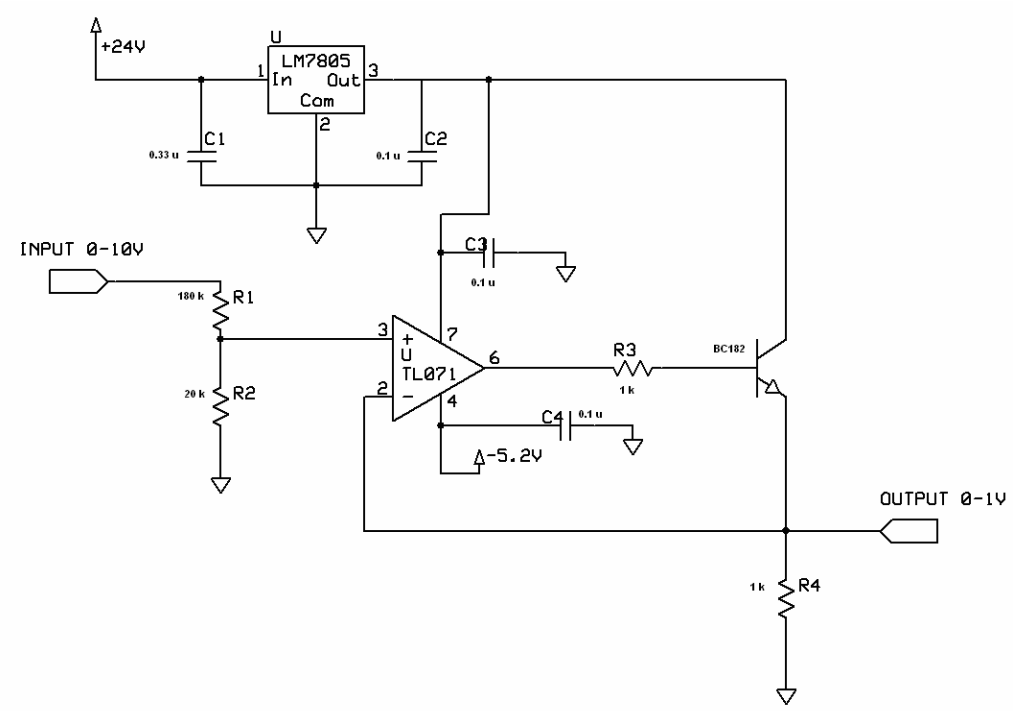


**Appendix Fig. 12. Schematics for the buffer amplifier. Voltages between 0 and 10 volts are taken from the DA output of the FPGA-card, and produce a control voltage between 0 and 1 V at the output.**

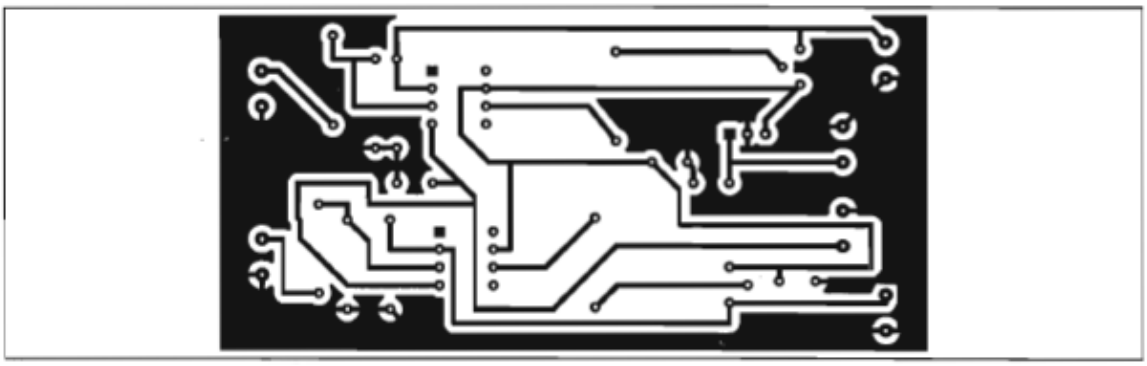

**Appendix Fig. 13. Printed circuit board for buffer amplifiers (5 cm × 16 cm)**

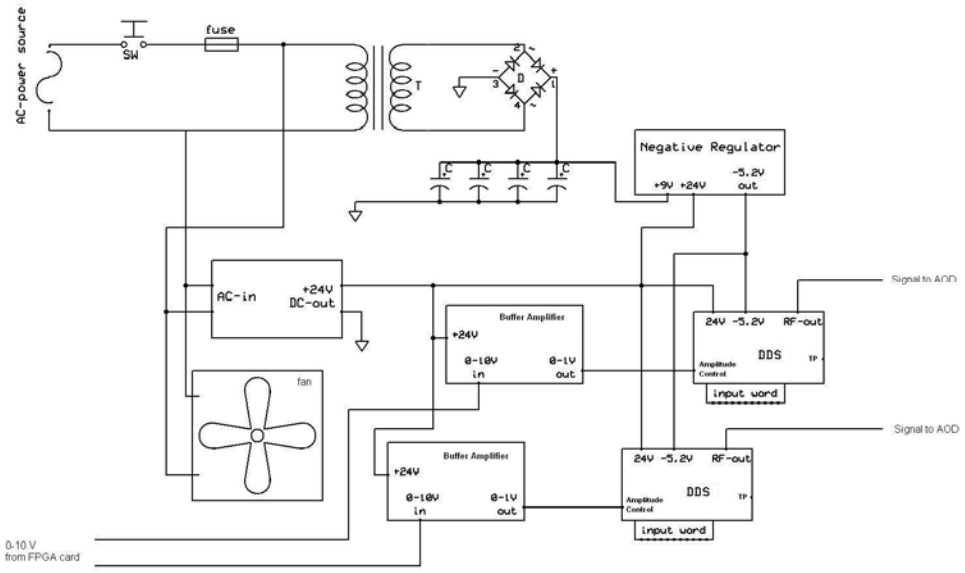


**Appendix Fig. 14. Diagram of the power source and buffer amplifiers for the DDSs. Power is drawn from a wall outlet, transformed, rectified and filtered with four 4700 µF capacitors before it is regulated to -5.2 volts. The figure also shows the cooling fan, buffer amplifiers and the +24 V voltage source. In the DDSs there are also test points (TP) where the RF output (attenuated by 20 dB) can be measured.**

# C. FPGA pin-outs

**Table 2. Pin out for the FPGA, a D-sub connector and a cable of 36 wires.**

| FPGA pin<br>on DIO1- and DIO2-connectors | D-connector pin number | DDS Function | Wire color (back/streak) |
|---|---|---|---|
| DIO0 | 1 | FS0 | brown/green |
| DIO2 | 2 | FS2 | white/yellow |
| DIO4 | 3 | FS4 | yellow/brown |
| DIO6 | 4 | FS6 | yellow/pink |
| DIO8 | 5 | FS8 | white/green |
| DIO10 | 6 | FS10 | green/black |
| DIO12 | 7 | FS12 | brown/red |
| DIO14 | 8 | FS14 | yellow/black |
| DIO16 | 9 | FS16 | green/blue |
| DIO18 | 10 | FS18 | yellow/blue |
| DIO20 | 11 | FS20 | yellow/red |
| DIO22 | 12 | FS22 | green/brown |
| DIO24 | 13 | FS24 | yellow/gray |
| DIO26 | 14 | FS26 | pink/green |
| DIO28 | 15 | FS28 | white/gray |
| DIO39 | 16 | Latch (active high) | white (no streak) |
| DIO38 | 17 | Master reset (active high) | brown (no streak) |
| N/C | 18 | N/C | pink (no streak) |
| DGND | 19 | Ground | yellow (no streak) |
| DIO1 | 20 | FS1 | gray/pink |
| DIO3 | 21 | FS3 | white/pink |
| DIO5 | 22 | FS5 | orange/blue |
| DIO7 | 23 | FS7 | pink/brown |
| DIO9 | 24 | FS9 | white/blue |
| DIO11 | 25 | FS11 | brown/blue |
| DIO13 | 26 | FS13 | gray/green |
| DIO15 | 27 | FS15 | brown/black |
| DIO17 | 28 | FS17 | white/black |
| DIO19 | 29 | FS19 | white/red |
| DIO21 | 30 | FS21 | gray/brown |
| DIO23 | 31 | FS23 | green (no streak) |
| DIO25 | 32 | FS25 | lilac (no streak) |
| DIO27 | 33 | FS27 | black (no streak) |
| DIO29 | 34 | FS29 | blue (no streak) |
| DIO37 | 35 | Enable (pulled up)<br>Disable = TTL low | orange (no streak) |
| N/C | 36 | N/C | N/C |
| N/C | 37 | Analog modulation (optional) | gray (no streak) |

**Table 3. All FPGA pin-outs for digital connector DIO. There is another connector with same pins for the other DDS. Five digital lines are free.**

| PIN# | DIO | function | PIN# | DIO | function | PIN# | DIO | function |
|---|---|---|---|---|---|---|---|---|
| 68 | DIO39 | Latch | 12 | DGND | | 1 | DGND | |
| 34 | DIO38 | Master reset | 46 | DIO11 | FS11 | 35 | DIO0 | FS0 |
| 67 | DIO37 | Disable | 13 | DGND | | 2 | DGND | |
| 33 | DIO36 | free | 47 | DIO12 | FS12 | 36 | DIO1 | FS1 |
| 66 | DIO35 | free | 14 | DGND | | 3 | DGND | |
| 32 | DIO34 | free | 48 | DIO13 | FS13 | 37 | DIO2 | FS2 |
| 65 | DIO33 | free | 15 | DGND | | 4 | DGND | |
| 31 | DIO32 | free | 49 | DIO14 | FS14 | 38 | DIO3 | FS3 |
| 64 | DIO31 | (discarded) | 16 | DGND | | 5 | DGND | |
| 30 | DIO30 | (discarded) | 50 | DIO15 | FS15 | 39 | DIO4 | FS4 |
| 63 | DIO29 | FS29 | 17 | DGND | | 6 | DGND | |
| 29 | DIO28 | FS28 | 51 | DIO16 | FS16 | 40 | DIO5 | FS5 |
| 62 | DIO27 | FS27 | 18 | DGND | | 7 | DGND | |
| 28 | +5V | | 52 | DIO17 | FS17 | 41 | DIO6 | FS6 |
| 61 | DIO26 | FS26 | 19 | DGND | | 8 | DGND | |
| 27 | +5V | 1 | 53 | DIO18 | FS18 | 42 | DIO7 | FS7 |
| 60 | DIO25 | FS25 | 20 | DGND | | 9 | DGND | |
| 26 | DGND | | 54 | DIO19 | FS19 | 43 | DIO8 | FS8 |
| 59 | DIO24 | FS24 | 21 | DGND | | 10 | DGND | |
| 25 | DGND | | 55 | DIO20 | FS20 | 44 | DIO9 | FS9 |
| 58 | DIO23 | FS23 | 22 | DGND | | 11 | DGND | |
| 24 | DGND | | 56 | DIO21 | FS21 | 45 | DIO10 | FS10 |
| 57 | DIO22 | FS22 | | | | | | |
| 23 | DGND | | | | | | | |

**Table 4. All FPGA pin-outs for analog connector MIO. There is one analog input, 6 analog outputs and 12 digital i/o lines free. (detector) indicates pins reserved for a second PSD.**

| PIN# | MIO | function | PIN# | MIO | function | PIN# | MIO | function |
|---|---|---|---|---|---|---|---|---|
| 68 | AI0+ | detector X | 12 | DIO12 | free | 1 | +5V | |
| 34 | AI0- | detector X | 46 | DIO13 | free | 35 | +5V | rotary cont |
| 67 | AIGND0 | | 13 | DIO14 | free | 2 | DGND | rotary cont |
| 33 | AIGND1 | | 47 | DIO15 | free | 36 | DIO0 | rotary cont |
| 66 | AI1+ | detector Y | 14 | AOGND7 | | 3 | DGND | |
| 32 | AI1- | detector Y | 48 | AO7 | free | 37 | DIO1 | rotary cont |
| 65 | AI2+ | detector Z | 15 | AOGND6 | | 4 | DGND | |
| 31 | AI2- | detector Z | 49 | AO6 | free | 38 | DIO2 | rotary cont |
| 64 | AIGND2 | | 16 | AOGND5 | | 5 | DGND | |
| 30 | AIGND3 | | 50 | AO5 | free | 39 | DIO3 | rotary cont |
| 63 | AI3+ | (detector) | 17 | AOGND4 | | 6 | DGND | |
| 29 | AI3- | (detector) | 51 | AO4 | free | 40 | DIO4 | free |
| 62 | AI4+ | (detector) | 18 | AOGND3 | | 7 | DGND | |
| 28 | AI4- | (detector) | 52 | AO3 | free | 41 | DIO5 | free |
| 61 | AIGND4 | | 19 | AOGND2 | | 8 | DGND | |
| 27 | AIGND5 | | 53 | AO2 | free | 42 | DIO6 | free |
| 60 | AI5+ | (detector) | 20 | AOGND1 | to buffer amp. | 9 | DGND | |
| 26 | AI5- | (detector) | 54 | AO1 | to buffer amp. | 43 | DIO7 | free |
| 59 | AI6+ | (detector) | 21 | AOGND0 | to buffer amp.1 | 10 | DIO8 | free |
| 25 | AI6- | (detector) | 55 | AO0 | to buffer amp. | 44 | DIO9 | free |
| 58 | AIGND6 | | 22 | NC | | 11 | DIO10 | free |
| 24 | AIGND7 | | 56 | AISENSE | | 45 | DIO11 | free |
| 57 | AI7+ | free | | | | | | |
| 23 | AI7- | free | | | | | | |

# D. Parameters for the fits

**Table 5. Parameters of Eq.20 that were fitted in to the data in Figure 22.**

| | D ($m^2/s$) | k/β (1/s) | τ (μs) |
|---|---|---|---|
| P=500 mW | $(6.25\pm0.03)\cdot10^{-13}$ | 2500±40 | 19.297±0.013 |
| P=100 mW | $(5.60\pm0.03)\cdot10^{-13}$ | 530±20 | 21.1±0.3 |

**Table 6. Feedback gain parameters of Eq. 20.**

| G | 100 | 200 | 300 | 400 |
|---|---|---|---|---|
| $K_p$(500 mW) | 10.27±0.05 | 20.54±0.05 | 25.59±0.03 | 24.46±0.02 |
| $K_p$(100 mW) | 7.14±0.10 | 11.08±0.13 | | |

# E. Miscellaneous

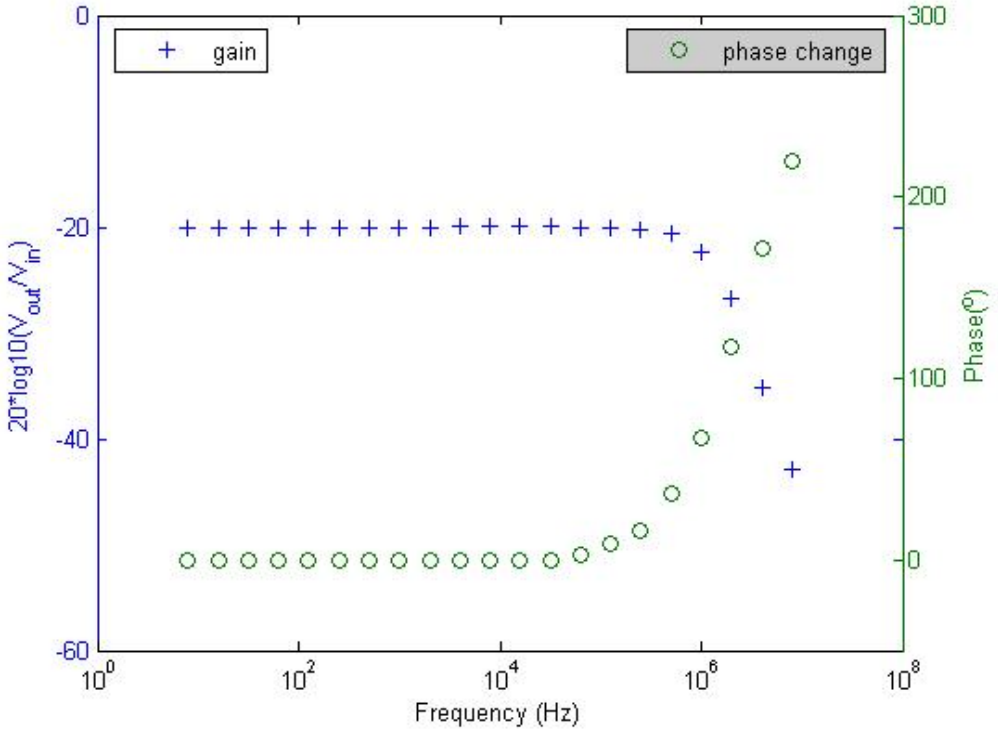


**Appendix Fig. 15. Gain and phase change of the buffer amplifiers. The design gain was -20 dB, to match the analog output (0-10 V) to the modulation input (0-1 V). The -23 dB point is at 1.17 MHz. Since the DA output of the FPGA runs at 1 MS/s the bandwidth of the amplifier is sufficient.**

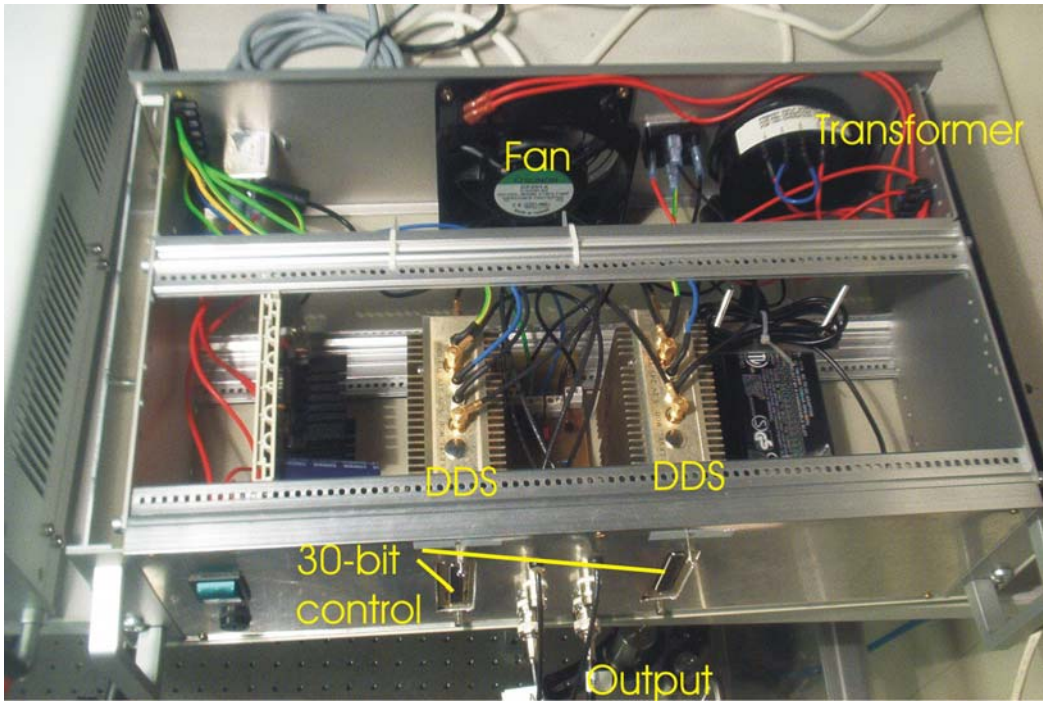


**Appendix Fig. 16. Image of the DDS box.**

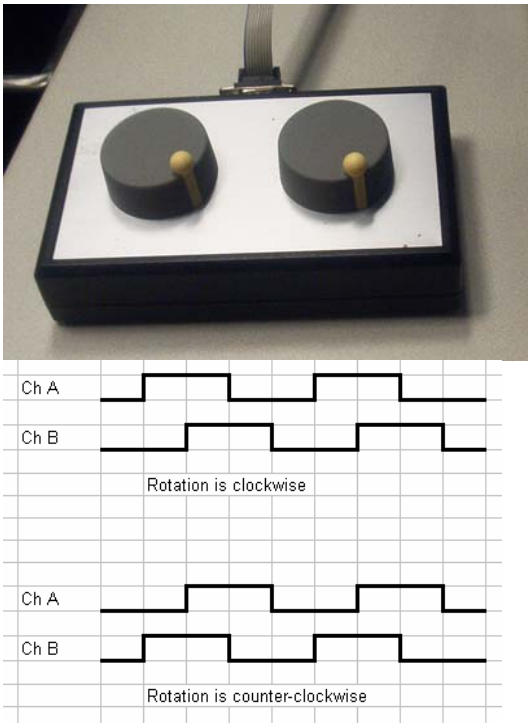


**Appendix Fig. 17. Magnetic rotary encoders and their signal.**